

CZECH TECHNICAL UNIVERSITY
IN PRAGUE

Faculty of Nuclear Sciences and Physical
Engineering
Department of Physics



Bachelor thesis

**Heavy Ion Physics at the ATLAS
experiment**

Oliver Matonoha

Supervisor: Ing. Olga Rusňáková, PhD.

Prague, 2016

ČESKÉ VYSOKÉ UČENÍ TECHNICKÉ
V PRAZE

Fakulta jaderná a fyzikálně inženýrská
Katedra fyziky



Bakalářská práce

**Fyzika těžkých iontů na experimentu
ATLAS**

Oliver Matonoha

Školitel: Ing. Olga Rusňáková, PhD.

Praha, 2016

Prohlášení:

Prohlašuji, že jsem svou bakalářskou práci vypracoval samostatně a použil jsem pouze podklady (literaturu, projekty, software, atd.) uvedené v příloženém seznamu.

Nemám závažný důvod proti užití tohoto školního díla ve smyslu § 60 Zákona č. 121/2000 Sb., o právu autorském, o právech souvisejících s právem autorským a o změně některých zákonů (autorský zákon).

V Praze dne

Oliver Matonoha

Title:

Heavy Ion Physics at the ATLAS experiment

Author: Oliver Matonoha

Specialisation: Experimental nuclear and particle physics

Sort of project: Bachelor thesis

Supervisor: Ing. Olga Rusňáková, PhD.

Abstract:

Heavy Ion Physics (HIP) is a field of particle physics studying collisions of heavy atomic nuclei at ultrarelativistic energies. One of the principal motivations for this is the possible creation of quark-gluon plasma (QGP) and its further analysis. QGP is an exotic form of matter, predicted by the theory of strong interaction (QCD) to exist under extreme conditions. In such, the normally bound quarks and gluons gain asymptotic freedom and can exist and travel unbound. It is also hypothesised to fill the universe in its earliest states. By researching the QGP behaviour, one can better understand the character of strong interaction.

The thesis' purpose is to acquaint oneself with the HIP and the ATLAS experiment and to conduct an analysis associated therewith. Reconstruction of the Υ quarkonia from data acquired at ATLAS in Pb+Pb collisions of $\sqrt{s_{\text{NN}}} = 2.76$ TeV in 2011 is presented. Dimuon decay channel was chosen in order to utilise ATLAS' great muon detection power. Cuts selection, regression analysis and division in centrality windows were performed. Clear suppression of Υ excited states is demonstrated, which is in consistency with the phenomenon of quarkonia melting and can be used to determine the QGP temperature.

Key words: heavy ion collisions, quark-gluon plasma, upsilon, quarkonium suppression, ATLAS

Název bakalářské práce:

Fyzika těžkých iontů na experimentu ATLAS

Autor: Oliver Matonoha

Obor: Experimentální jaderná a částicová fyzika

Školitel: Ing. Olga Rusňáková, PhD.

Abstrakt:

Fyzika těžkých iontů (HIP) je oborem částicové fyziky studující srážky těžkých atomových jader při ultrarelativistických energiích. Jednou z hlavních motivací je možné vytvoření quark-gluonového plasmatu (QGP) a jeho další zkoumání. QGP je exotická forma hmoty, která dle teorie silné interakce (QCD) může existovat za extrémních podmínek. Při nich získávají standardně vázané kvarky a gluony asymptotickou volnost a mohou se vyskytovat volné. Předpokládá se, že QGP tvořilo vesmír v jeho raných momentech. Zkoumání chování QGP může vést k lepšímu pochopení charakteru silné interakce.

Cílem práce je seznámit se s HIP a experimentem ATLAS a provést s tím související analýzu. Presentována je rekonstrukce kvarkonií Υ z dat nasbíraných na ATLASu v Pb+Pb srážkách při $\sqrt{s_{NN}} = 2.76$ TeV z roku 2011. Pro studium byl zvolen dvoumionový rozpadový kanál, který lze detektorem ATLAS velmi dobře měřit. Taktéž se provedla selekce cutů, regresní analýza a rozdělení dle centrality. Lze pozorovat viditelné potlačení excitovaných stavů Υ , což je v souladu s jevem zvaným tání kvarkonií. To lze použít k určení teploty QGP.

Klíčová slova: srážky těžkých iontů, quark-gluonové plasma, upsilon, potlačení kvarkonií, ATLAS

Acknowledgement

I have been greatly fortunate to be supervised by Dr. Rusňáková and for this I owe her many thanks. Her words of praise have always kept me motivated and made the analysis very entertaining. I am beyond appreciative of the opportunities she provided me with, her kind-hearted approach, and patience.

I would also like to express my heartfelt gratitude towards my parents. They have always supported me, never had any doubts and I could never pursue my passion if it was not for them.

Furthermore, I am deeply grateful to Dr. Bielčík for his assistance and care about my future as a scientist. I am also thankful towards Dr. Chaloupka for his valuable counsel, contagious enthusiasm and friendly approach. Finally, I would like to acknowledge Ing. Gallus who kindly provided me with the data and made the entire analysis possible in the first place.

Contents

| | |
|--|-----------|
| Introduction | 1 |
| 1 Introduction to particle physics | 3 |
| 1.1 Standard Model | 3 |
| 1.1.1 Matter particles | 4 |
| 1.1.2 Force carrier particles | 5 |
| 1.2 Quark-gluon plasma | 7 |
| 1.3 Heavy nuclei collisions | 7 |
| 1.3.1 Kinematic variables | 7 |
| 1.3.2 Centrality, impact parameter | 9 |
| 1.3.3 Nuclear modification factor | 11 |
| 2 Heavy quarkonia | 13 |
| 2.1 Properties of heavy quarkonia | 13 |
| 2.1.1 Families | 13 |
| 2.1.2 $Q\bar{Q}$ potential | 14 |
| 2.2 Production models | 16 |
| 2.2.1 Colour Evaporation Model | 17 |
| 2.2.2 Colour Singlet Model | 17 |
| 2.2.3 Colour Octet Model + NRQCD | 18 |
| 2.3 Quarkonia suppression | 18 |
| 2.3.1 Screening in the QGP | 18 |
| 2.3.2 Other production affecting phenomena | 19 |
| 2.4 Decay channels and feed-down | 21 |

| | | |
|----------|--|-----------|
| 3 | Recent results in Υ studies | 23 |
| 3.1 | LHC | 23 |
| 3.1.1 | ALICE | 24 |
| 3.1.2 | ATLAS | 29 |
| 3.1.3 | CMS | 32 |
| 3.2 | RHIC | 34 |
| 3.2.1 | STAR and PHENIX | 34 |
| 4 | ATLAS experiment | 37 |
| 4.1 | Large Hadron Collider | 37 |
| 4.2 | Experiment's overview | 39 |
| 4.3 | Inner detector | 41 |
| 4.3.1 | Pixel detector | 43 |
| 4.3.2 | Semiconductor tracker | 43 |
| 4.3.3 | Transition radiation tracker | 45 |
| 4.4 | Calorimeters | 45 |
| 4.4.1 | Electromagnetic calorimeter | 46 |
| 4.4.2 | Hadronic calorimeter | 46 |
| 4.5 | Muon spectrometer | 46 |
| 4.5.1 | Monitored Drift Tubes | 48 |
| 4.5.2 | Cathode-strip Chambers | 49 |
| 4.5.3 | Resistive Plate Chambers | 49 |
| 4.5.4 | Thin Gap Chambers | 49 |
| 5 | Author's analysis on $\Upsilon \rightarrow \mu^+\mu^-$ | 51 |
| 5.1 | Means for analysis | 52 |
| 5.1.1 | Data | 52 |
| 5.1.2 | ROOT framework | 52 |
| 5.2 | Invariant mass reconstruction | 52 |
| 5.2.1 | Methodology | 53 |
| 5.2.2 | Cuts analysis | 53 |
| 5.3 | Result of the $m_{\mu^+\mu^-}$ spectrum | 58 |
| 5.4 | Centrality dependence | 59 |

| | |
|--|-----------|
| 5.5 Outlook on further work | 62 |
| Conclusion | 65 |
| References | 67 |
| Appendix | I |
| A Fit results | I |
| B Staco reconstructed quantities | II |
| C η vs. $ \vec{p} $ | III |
| D Cuts on p_T | IV |

List of Figures

| | | |
|------|---|----|
| 1.1 | Particles in SM | 4 |
| 1.2 | Space-time evolution of A+A collision | 8 |
| 1.3 | Multiplicity and centrality | 10 |
| 2.1 | Charmonia and bottomonia families | 15 |
| 2.2 | Quarkonium potential | 16 |
| 2.3 | Quarkonia melting temperatures | 20 |
| 3.1 | Υ at ALICE in Pb+Pb | 25 |
| 3.2 | R_{AA} dependence on $\langle N_{\text{part}} \rangle$ at ALICE in Pb+Pb | 26 |
| 3.3 | R_{AA} dependence on y at ALICE in Pb+Pb | 27 |
| 3.4 | Υ at ALICE in p+Pb | 28 |
| 3.5 | R_{pPb} dependence on y at ALICE in p+Pb | 29 |
| 3.6 | Υ at ATLAS in p+Pb and p+p | 31 |
| 3.7 | R_{pPb} dependence on y^* in p+Pb at ATLAS | 31 |
| 3.8 | Υ at CMS in p+p and Pb+Pb | 33 |
| 3.9 | Υ from μ at STAR in Au+Au | 35 |
| 3.10 | Υ from e at STAR in Au+Au and d+Au | 36 |
| 3.11 | R_{dAu} dependence on y and $\langle N_{\text{part}} \rangle$ and R_{AA} dependence on $\langle N_{\text{part}} \rangle$ at STAR and PHENIX | 36 |
| 4.1 | CERN accelerator complex | 38 |
| 4.2 | Overview of ATLAS | 40 |
| 4.3 | Particle propagation in ATLAS | 41 |
| 4.4 | Inner Detector layout | 42 |
| 4.5 | Inner Detector geometry | 44 |

| | | |
|-----|--|----|
| 4.6 | ATLAS calorimeters | 47 |
| 4.7 | ATLAS muon spectrometer | 48 |
| 5.1 | Invariant mass spectrum with J/ψ and $\Upsilon(1S)$ | 54 |
| 5.2 | Track quality values | 56 |
| 5.3 | Muon dynamics distribution | 57 |
| 5.4 | Υ invariant mass spectrum with fit | 59 |
| 5.5 | Centrality in HI at ATLAS | 60 |
| 5.6 | Distribution for ΣE_T | 60 |
| 5.7 | CMS results of centrality dependence of R_{AA} | 61 |
| 5.8 | Υ invariant mass spectrum in different centralities | 63 |

Introduction

Equipped with his five senses, man explores the universe around him and calls the adventure Science.

—Edwin Powell Hubble

Exploration has always been one of the most driving interests of humanity. Astronomers look for objects in the big black unknown, philosopher seek the purpose of living, and particle physicists explore the very substance of which reality is built.

One of the most alluring subjects of today particle physics is examination of the quark-gluon plasma (QGP). It is an absolutely singular state of matter believed to fill the universe very shortly after the Big Bang. Such medium can come into existence only under extreme conditions. Physicists attempt to reproduce these by colliding heavy ions (HI) at speed very close to the speed of light.

The objective of this bachelor thesis is to acquaint the reader with these collisions studies, to review the physics of heavy quarkonia (and its application to probe the QGP), as well as to introduce the detection apparatus.

Later in the thesis, the author's original analysis on the production of Υ quarkonia from dimuon decay is presented. Data from the ATLAS experiment at LHC in CERN were chosen. This is interesting, because unlike the ALICE or the STAR experiments, ATLAS is not primarily used for HI physics. Be that as it may, the ATLAS' prominent muon spectrometer makes it a great candidate for considered analysis.

Chapter 1

Introduction to particle physics

Efforts to discover the basic building substance span as far as into Ancient Greece. Whereas Thales thought everything is composed of water and Pythagoras deemed it to be numbers, Demokritos proposed the idea of matter consisting of atoms, indivisible building blocks. More than two thousand years later, this premise was further developed by the discovery of atoms being formed by nucleons and electrons. Later, quarks and other particles were found.

Nowadays, we now believe there are 17 different elementary particles, some of which are stable and group together to form matter, whilst other are more exotic and can be found only by elaborate means. They have a solid theoretical background for their existence stemming from what we call the Standard Model.

1.1 Standard Model

Endeavours to describe the ultimately structureless constituents of matter and the interactions acting between them resulted in the creation of the Standard Model of particle physics by various scientists in the early 1970s. It was constructed on adequate fields of quantum mechanics, quantum field theory, special relativity, and electromagnetism. It has been successful in explanation of numerous phenomena and its predictions have been seen in most experimental results. Most predicted particles have been successfully observed. Particularly,

1.1. STANDARD MODEL

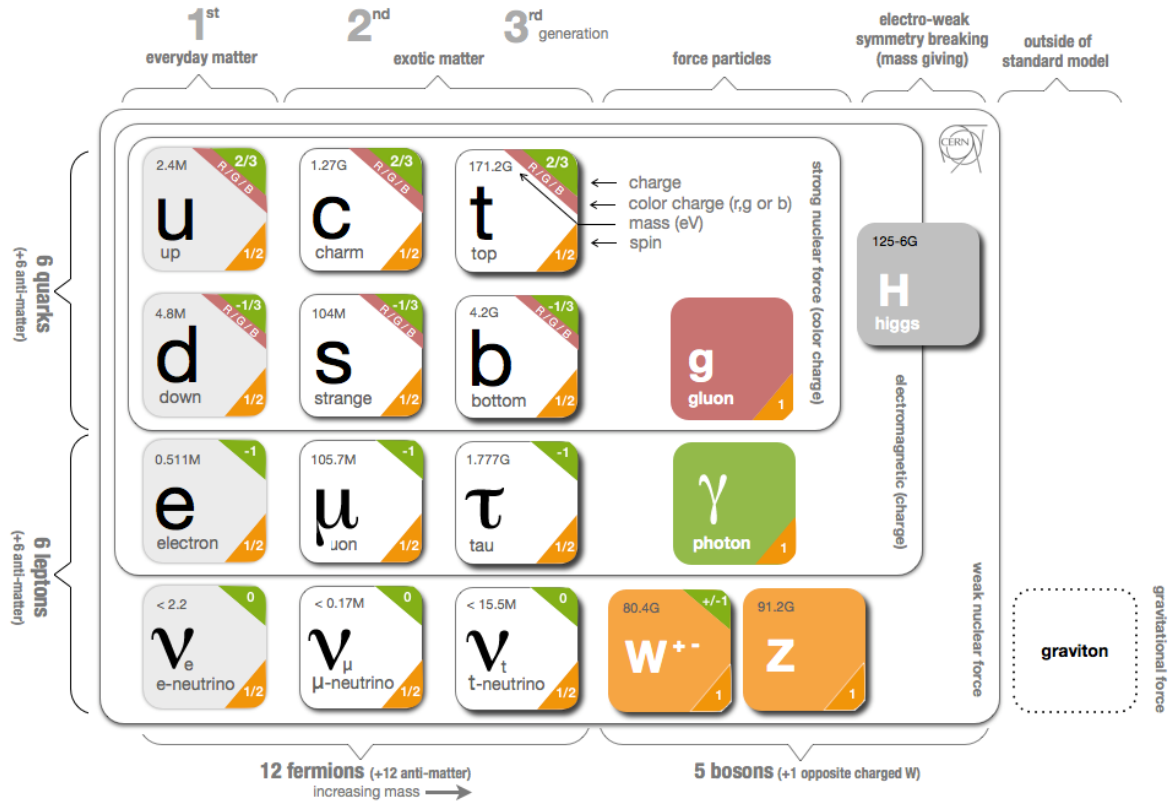


Fig. 1.1: Elementary particles consistent with the Standard Model. Taken from [2].

the discovery of the Higgs boson at LHC in 2012 gave it further credence [1].

Nonetheless, the Standard Model remains unsuccessful in answering the questions of why was there more matter than antimatter created in the Big Bang, or what is the dark matter, which is seemingly responsible for holding the universe together. Moreover, it completely omits the effects of gravitational force due to its negligibility on particle physics scales.

1.1.1 Matter particles

According to the Standard Model, all matter observed by man consists of few fundamental particles, which group together to build everything around us. Primarily, they can be divided into two categories - quarks and leptons. Within each category, they occur in three pairs

(generations), with each generation being non-linearly heavier (and also less stable) than the previous. The types of particles are called *flavours*. Each of these particles also exist in their antimatter counterpart.

Quarks consist of: up, down (first generation); charm, strange (second generation); bottom, top (third generation). Quarks hold non-integer electric charge, have $\frac{1}{2}$ spin and are also, uniquely to them, characterised by 'colour charge'. Due to this, quarks interact via the strong interaction and, normally, cannot exist separated - they always bind together to form particles called hadrons. Formations of three quarks are named baryons (these are e.g. protons or neutrons), formations of a quark and an antiquark are called mesons. Special case of mesons are the quarkonia, wherein the quark and the antiquark are of the same flavour. More exotic hadron types also exist, such as the pentaquark, discovered in 2015 [3].

Each **lepton** generation includes a charged lepton and a respective neutrino. Hence, there are: electron, electron neutrino (first generation); muon, muon neutrino (second generation); tauon, tauon neutrino (third generation). Leptons also have $\frac{1}{2}$ spin, but only the charged leptons carry electric charge. Neutrino masses are extremely small, nonetheless, in 2015, a discovery was made proving that this mass is non-zero.

1.1.2 Force carrier particles

Besides the matter particles, Standard Model also introduces a second set of particles - force carriers (also called gauge bosons). An interaction between two particles is carried out by the exchange of these. Each fundamental force is mediated by the means of different gauge bosons. Photons carry out the effects of electromagnetic force and are massless. Gluons convey the strong interaction and are, also, massless. Weak interaction is realised through the Z and W bosons, which have finite masses.

Strong interaction is the most potent of all interactions. It is responsible for holding hadrons as well as whole nuclei together. Despite gluons being massless, strong interaction has limited reach. Only quarks and gluons are affected by the strong force. Quarks are not observed unbound. Nevertheless, scattering experiments showed that quarks move almost

1.1. STANDARD MODEL

freely within the nucleus. These phenomena are called the quark confinement and asymptotic freedom. In analogy to electric charge, we say the quarks and gluons carry a colour charge. There are red, green, blue, antired, antigreen, and antiblue charges. A bound state can form a hadron, only if the resulting colour is *white*, also called a colour singlet state. The other, colour octets, are forbidden. The theory of strong interaction is called quantum chromodynamics (QCD).

Electromagnetic interaction is the best described. It has unlimited reach and its magnitude follows the Coulomb law. It is responsible for keeping the electrons on their orbits and molecules formations. All electrically charged particles are subjected to the electromagnetic force. Electromagnetic field is well described by the Maxwell equations. The theory of electromagnetic force on particle physics scales is called quantum electrodynamics (QED).

As name suggests, the **weak interaction** is the weakest force of SM and, also, has limited reach. Via the weak interaction, quarks and leptons can change their flavour. As a result of it, for instance, beta decays exist. It is the only force which acts upon neutrinos. The weak force can be described within QED through the Glashow-Weinberg-Salam electro-weak (EW) unification.

Gravitational force is not described within the Standard Model, however, is thought to be mediated by a graviton - a 2 spin particle which yet remains to be discovered.

Lastly, besides the matter particles and gauge bosons, a Higgs boson forms a category of its own. In the Higgs mechanism, it is introduced as a quantum of the Higgs field, via which particles gain their masses.

Looking at the particles from the perspective of statistical physics, quarks and leptons are fermions and force carriers are bosons. Fermions, unlike bosons, follow the Pauli's exclusion principle. It states that any two particles cannot exist in the same state (energy, spin, charge...) in the system at the same time. In the words of quantum physics, it says that they cannot be described by the same quantum numbers.

1.2 Quark-gluon plasma

When large amount of energy is deposited in small amount of space, the temperature is sufficient for the quarks and gluons to break their bindings and exist freely. As such, they form a new state of matter called the quark gluon plasma. It is generally believed that the universe was in this state of matter few picoseconds after the Big Bang. Studying the QGP is absolutely vital since it might provide insight on the evolution of universe.

Conditions for QGP existence are realised in heavy nucleus–nucleus collisions. For instance, at LHC energies of ~ 3 TeV per nucleon, up to 1262 TeV of energy can be deposited in a minuscule region of few fm [7]. This leads to the presence of extremely high energy density. Such conditions are favourable for the creation and existence of the QGP, for a short time. Then, as it chills out, a gas of hadrons is formed, which further disperses into countless other particles which reach the detectors. Space-time evolution of the collision is depicted in Fig. 1.2.

Since the conditions for the QGP are so rare to achieve and exist only for an extremely limited amount of time, it is very difficult to study and indirect sophisticated methods evaluating its remnants have to be used. Some of these are: jet quenching, quarkonia suppression, thermal radiation, collective flow, dilepton enhancement. The phenomenon of quarkonia suppression is elaborated on in Chapter 2.

1.3 Heavy nuclei collisions

1.3.1 Kinematic variables

For the sake of conciseness, one uses *natural units* in particle physics problems by setting basic constants (c , \hbar) equal to 1. In order to describe particles with speeds approaching the speed of light, relativistic method need to be used. Thus, one uses Lorentz *four-vectors*, such as $\mathbf{x} = (t, x, y, z)$ or $\mathbf{p} = (E, p_x, p_y, p_z) = (E, \vec{p}_T, p_{\parallel})$. Their squares remain invariant in Lorentz transformation.

1.3. HEAVY NUCLEI COLLISIONS

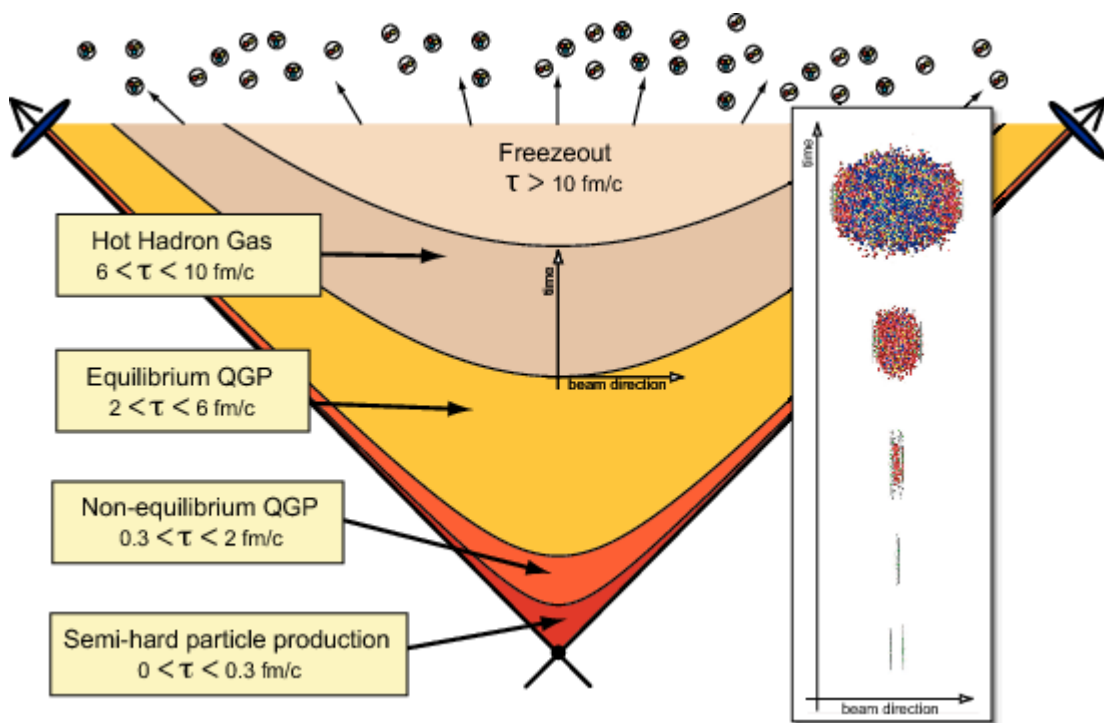


Fig. 1.2: Space-time evolution of a nucleon-nucleon collision. Visualisation of the collision is also shown. Taken from [4].

Furthermore, one uses certain variables due to their convenience in particle physics. One of these is the *transverse energy* E_T . It is Lorentz invariant and depends on the rest mass of the particle and its transverse momentum:

$$E_T^2 = E^2 - p_z^2 = \vec{p}_T^2 + m^2 . \quad (1.1)$$

It is also useful to define *rapidity*, a variable describing particle's longitudinal velocity. Even though it is not Lorentz invariant, it transforms additively under Lorentz boosts, unlike velocity:

$$y = \frac{1}{2} \log \frac{1 + \beta}{1 - \beta} . \quad (1.2)$$

One can use two decent approximations for rapidity [6]. Firstly, for very small longitudinal velocities, rapidity is approximately equal to β ($y \approx \beta$). Secondly, for a particle with momentum very high with respect to its mass ($p > m$), one can relate the rapidity to the *emission (polar) angle* of the particle θ , via another variable, *pseudorapidity* η :

$$\eta = -\log \left(\tan \frac{\theta}{2} \right) \approx y . \quad (1.3)$$

Altogether, along with the *azimuthal angle* ϕ , pseudorapidity η and transverse momentum \vec{p}_T , entire collision geometry can be described by the means of following relations:

$$\begin{aligned} p_x &= \vec{p}_T \cos \phi , \\ p_y &= \vec{p}_T \sin \phi , \\ p_z &= |\vec{p}| \sinh \eta . \end{aligned} \quad (1.4)$$

1.3.2 Centrality, impact parameter

A nucleus-nucleus collision can be characterised by an impact parameter b . This is the relative distance between the nuclei centers at the point of impact. The b can span from 0 (central

1.3. HEAVY NUCLEI COLLISIONS

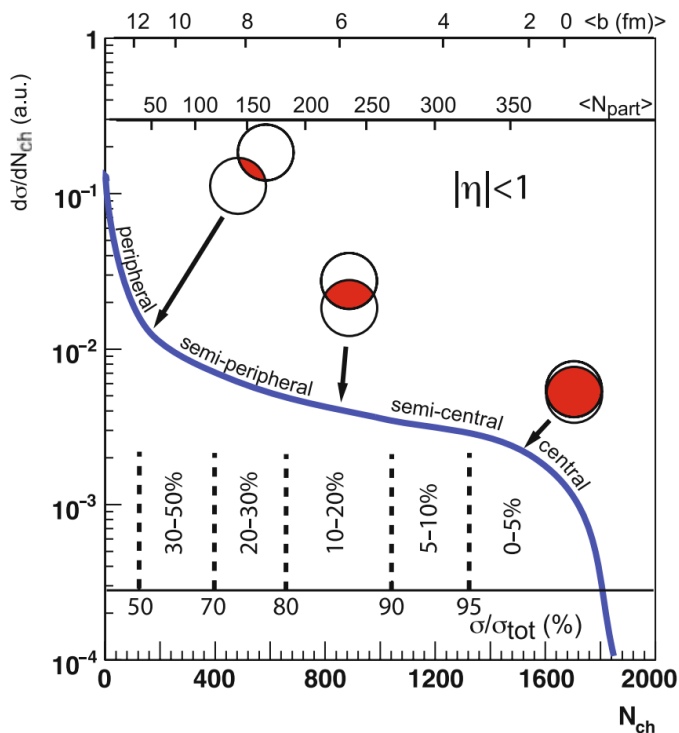


Fig. 1.3: Cartoon of a distribution in final-state particle multiplicity. Connections with centrality, b , and $\langle N_{\text{part}} \rangle$ can be seen. Taken from [4].

collision) to $R_1 + R_2$ (peripheral), where R_1, R_2 are the nuclei' radii.¹ The centrality of the collision then determine the amount of energy deposited in the event.

The b is not a measurable physical quantity. Therefore, it is calculated indirectly — either via inclusive product particle multiplicity or the total transverse energy of the event. A cartoon illustrating the distribution in final multiplicity N_{ch} and its correlation with b , centrality, and the number of nucleons actively participating in the collision $\langle N_{\text{part}} \rangle$ is shown in Fig. 1.3.

¹However, at some experiments, the so called *ultra-peripheral* collisions are measured, wherein $b > R_1 + R_2$ and the nuclei just miss each other.

1.3.3 Nuclear modification factor

In heavy ion collisions, one often studies yields of certain produced particles and compares them with the produced amounts in p+p collisions. This can deliver substantial information about the QGP medium created in HI collisions. This change in production is often quantified by the means of nuclear modification factor R_{AA} . In its simplest form, it can be defined as

$$R_{AA} = \frac{N_{AA}}{N_{\text{coll}} \times N_{\text{pp}}} , \quad (1.5)$$

where N_{AA} , N_{pp} are the normalised yields of the given particle in HI and p+p collisions, respectively, and N_{coll} is the average number of participant nucleons binary collisions.

In practice, this ratio is calculated in a more sophisticated manner, often via the use of production cross sections.

Chapter 2

Heavy quarkonia

This chapter's purpose is to review the theoretical background on heavy quarkonia properties and behaviour. The quarkonia families will be presented, as well as the motivation for studying them, as was first proposed by Matsui and Satz [8].

2.1 Properties of heavy quarkonia

Quarkonia are a special case of mesons, in which the quark and the anti-quark are of the same flavour. When talking about heavy quarkonia, this flavour is *charm* or *bottom*.¹ They usually have smaller radii than other mesons and thus, they react less significantly via the strong force with other hadrons in the medium. Thanks to their behaviour and easily detectable decay products, quarkonia are great candidates for studies of QCD medium.

2.1.1 Families

The bound states of $c\bar{c}$ and $b\bar{b}$ pairs are also referred to as *charmonia* and *bottomonia*, respectively. The charmonia and bottomonia families are represented by a variety of states, which differ in quantum numbers of the bound system. The most tightly bound states are the J/ψ - a $c\bar{c}$ pair of mass ~ 3.1 GeV, and the $\Upsilon(1S)$ - a $b\bar{b}$ pair of mass ~ 9.5 GeV. They are

¹The $t\bar{t}$ pair does not form a bound state due to its extreme mass.

2.1. PROPERTIES OF HEAVY QUARKONIA

| States | J/ψ | χ_c | ψ' | $\Upsilon(1S)$ | χ_b | $\Upsilon(2S)$ | χ'_b | $\Upsilon(3S)$ |
|----------------------|----------|----------|---------|----------------|----------|----------------|-----------|----------------|
| Mass [GeV] | 3.07 | 3.53 | 3.68 | 9.46 | 9.99 | 10.02 | 10.26 | 10.36 |
| Binding energy [GeV] | 0.64 | 0.20 | 0.05 | 1.10 | 0.67 | 0.54 | 0.31 | 0.20 |
| Radius [fm] | 0.25 | 0.36 | 0.45 | 0.14 | 0.22 | 0.28 | 0.34 | 0.39 |

Tab. 2.1: Mass, binding energy, and radii of common quarkonia states of charm and bottom family. Taken from [4].

the most studied states. Heavier ones, namely ψ' , $\Upsilon(2S)$, $\Upsilon(3S)$, are also often analysed. For the quarkonia basic properties, see Tab. 2.1. Schematics of the charmonia and bottomonia states can be found in Fig. 2.1.

2.1.2 $Q\bar{Q}$ potential

Let us consider a two-body system of a quark and an antiquark of the same flavour in no medium, i.e. $T = 0$. If the relative distance is r , then the colour potential of said pair takes the form of

$$V(r, T = 0) = \kappa r - \frac{4\alpha_s}{3} \cdot \frac{1}{r}, \quad (2.1)$$

where κ is the string tension coefficient and α_s the strong coupling constant. The first term is linear and corresponds to the confining properties of the strong interaction. The second term is Coulomb-like and determines the character of the potential at short distances. It comes from the gluon exchange nature of the strong interaction between the Q and \bar{Q} . This potential is simplified and omits the spin-orbit and spin-spin couplings, which allow us to distinguish additional states [6].

To continue, let us now put the same system into a QCD medium of finite temperature T . The confining term loses its influence and fully diminishes at QGP temperatures. The Coulomb-like part is also modified, into a Yukawa-like form, to account for the fact that the Q and \bar{Q} colour charges are now screened by the vast amount of free quarks and gluons in

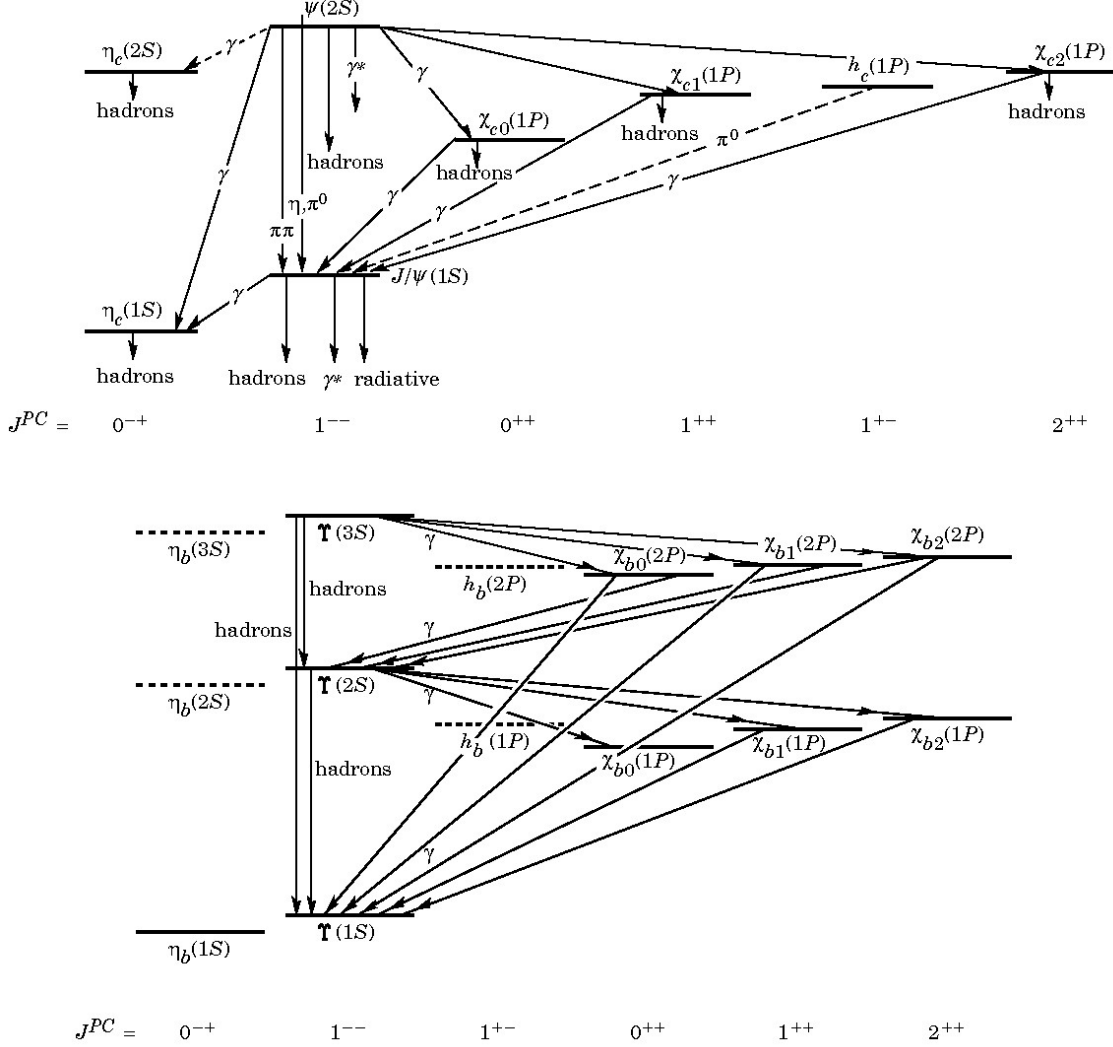


Fig. 2.1: Diagrams of the bound states of the charmonia family (up) and the bottomonia family (down). The ψ' state is denoted as $\psi(2S)$. Vertical position of the bound states indicates their mass. Quantum numbers are shown at the bottom of each diagram. Decay modes of the states are also displayed. Taken from [5].

2.2. PRODUCTION MODELS

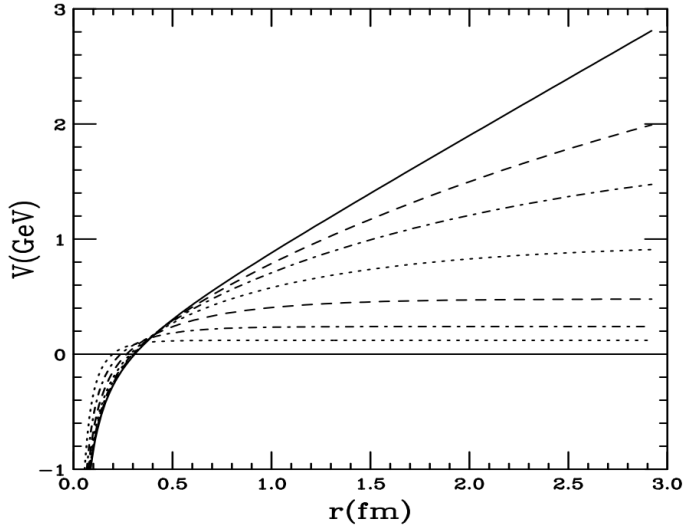


Fig. 2.2: The heavy quarkonium potential from Eq. (2.2) as function of r for different medium temperatures T . The thick solid line denotes the standard $T = 0$ potential, $r_D(T) \rightarrow \infty$, the other lines show the function for finite values of $r_D(T)$. Taken from [6].

the medium [7]. The modified potential now goes as follows,

$$V(r, T) = \kappa r_D (1 - e^{-\frac{r}{r_D}}) - \frac{4\alpha_s}{3} \cdot \frac{e^{-\frac{r}{r_D}}}{r}, \quad (2.2)$$

where $r_D = r_D(T)$ is the Debye radius, which characterises the screening effect, and is inversely proportional to the medium temperature. The potential (2.2) as function of separation distance r is displayed in Fig. 2.2.

2.2 Production models

Whilst it is relatively easy to calculate the production of heavy quarks, the production of the actual bound quarkonia proves to be challenging. First off all, the resulting hadrons need to be colour singlets (colourless), however, most of the $Q\bar{Q}$ are produced as colour octets. Models have been developed in order to describe the process of hadronisation of the $Q\bar{Q}$ pair.

2.2.1 Colour Evaporation Model

The Colour Evaporation Model (CEM) is a phenomenological model and succeeds well in describing experimental results on inclusive quarkonia cross section spectra. It assumes that each $Q\bar{Q}$ pair, whose mass is lesser than twice the mass of the lightest open heavy-flavour meson (m_H , i.e. m_D or m_B), evolves into a quarkonium. As such, it neglects the variation in colour, angular momentum and spin states of the pairs. According to the model, these quantum states of the $Q\bar{Q}$ pair at the point of its hadronisation are not correlated to the quantum states at its production, due to the occurrence of soft gluon emissions in between.

The total cross section of a quarkonium state Q is then expected to be directly related to the cross section of the $Q\bar{Q}$ pair production, integrated in said region, multiplied by a statistical factor F_Q , which represents the probability of the actual state to be hadronised.

$$\sigma_Q = F_Q \cdot \int_{2m_q}^{2m_H} \frac{d\sigma_{Q\bar{Q}}}{dm_{Q\bar{Q}}} dm_{Q\bar{Q}} \quad (2.3)$$

The probability factor is given as $F_Q = \frac{1}{9} \cdot \frac{2J_Q+1}{\sum_i 2J_i+1}$, where the sum runs over all possible quarkonia states in said region and J_i is their respective spin. The first term is given by the assumption that only one (singlet) colour state out of nine possible is allowed in hadronisation. The second term is a ratio of the amounts of quarkonia spin eigenstates [9].

2.2.2 Colour Singlet Model

Opposite to the CEM assumption, the Colour Singlet Model (CSM) forbids the evaporation of a $Q\bar{Q}$ pair's colour and spin quantum states via the soft gluon emission, which is expected to be notably suppressed. Hence, in order to hadronise into a quarkonia state, the produced $Q\bar{Q}$ pair must already have proper quantum number and be a colour singlet.

The model was developed shortly after J/ψ discovery. It is calculated by perturbative QCD theory and uses the expansion in strong coupling constant α_s . It has significant predictive power, e.g. it can give information about the quarkonium polarisation. Nonetheless, it fails to describe cross section spectra at higher energies [6].

2.3. QUARKONIA SUPPRESSION

2.2.3 Colour Octet Model + NRQCD

The Colour Octet Model assumes that it is, too, possible for colour octet $Q\bar{Q}$ states to hadronise into a quarkonium. The colour neutralisation occurs during the formation by an emission of gluon. The model is built on a field theory Non-relativistic QCD (NRQCD). This theory allows us to utilise combination of two approaches, pQCD in short distance/high momentum region and nonperturbative QCD in long distance/low momentum region. This is called *factorisation* and allows us to account for more effects associated with the dynamics of $Q\bar{Q}$ binding [6].

Although there are some discrepancies when comparing with experimental results, the COM is arguably the most appealing approach [6].

2.3 Quarkonia suppression

2.3.1 Screening in the QGP

The colour potential of a quarkonium in QCD medium of temperature T takes on the form of (2.2). Effective range of this potential is given by the Debye radius r_D . Beyond this distance, the attractive interaction loses its effect. Since $r_D \propto \frac{1}{T}$, at sufficiently high temperatures, the range becomes smaller than the actual diameter of the $Q\bar{Q}$ state, which causes it to *melt*. The heavy quark and antiquark then combine with other quarks of the medium during the hadronisation process to form other heavy mesons [7].

In a heavy ion collision, the $Q\bar{Q}$ quarkonium is created in the first stages, via hard processes with high energy transfers, due to their high mass. If a QGP is, subsequently, produced in its vicinity, the screening effect of the plasma will modify the potential, causing the $Q\bar{Q}$ melting. The final observer yield of the quarkonia states is then to be considerably *suppressed* with respect to the scenario of no QGP creation [7].

For specific estimation, let us consider the system Hamiltonian

$$H = \frac{p^2}{2m_{\text{red}}} + \kappa r_D (1 - e^{-\frac{r}{r_D}}) - \frac{4\alpha_s}{3} \cdot \frac{e^{-\frac{r}{r_D}}}{r}, \quad (2.4)$$

where $m_{\text{red}} = \frac{1}{2}m_Q$ is the reduced mass of the system. Using the uncertainty relation $\langle p^2 \rangle \langle r^2 \rangle \sim 1$, the Hamiltonian gives us the system's energy $E(r)$. Minimising E in r gives us the diameter $r_{Q\bar{Q}}$ of the $Q\bar{Q}$ state at given T . More precise calculations are obtained from adequate Schrödinger equation. For values of r_D lower than $r_{Q\bar{Q}}$, the $E(r)$ does not have a minimum and the bound state dissociates [6].

The Debye screening radius can be determined from pQCD. For a medium of quarks with 3 colours and 3 flavours, it goes as follows,

$$r_D(T) = \sqrt{\frac{2}{3g^2}} \frac{1}{T}, \quad (2.5)$$

where $g^2 = 4\pi\alpha_s$. Since r_D is temperature dependent and $r_{Q\bar{Q}}$ varies for each quarkonium states, one can study suppression of different states and use the condition $r_{Q\bar{Q}} < r_D$ to determine the medium's temperature (i.e. larger quarkonia melt at lower temperatures). Ratios of the melting temperature of the quarkonium T and the QGP critical temperature T_C , as calculated by various models (far more complex than what is shown here), can be found in Fig. 2.3.

2.3.2 Other production affecting phenomena

2.3.2.1 Statistical recombination

Statistical recombination, also called regeneration, is the process of creating the quarkonium state not by the hard processes in the beginning, but by random merge during the hadronisation stage. Therefore, its probability is directly proportional to the number of q and \bar{q} pairs in the medium and leads to an *enhancement* of the total $Q\bar{Q}$ yield. As seen in Tab. 3.1, the number of $c\bar{c}$ and $b\bar{b}$ pairs, $\propto \frac{1}{2}(\# \text{ of quarks})^2$, becomes non-negligible at high energies, especially in the charm case.

2.3. QUARKONIA SUPPRESSION

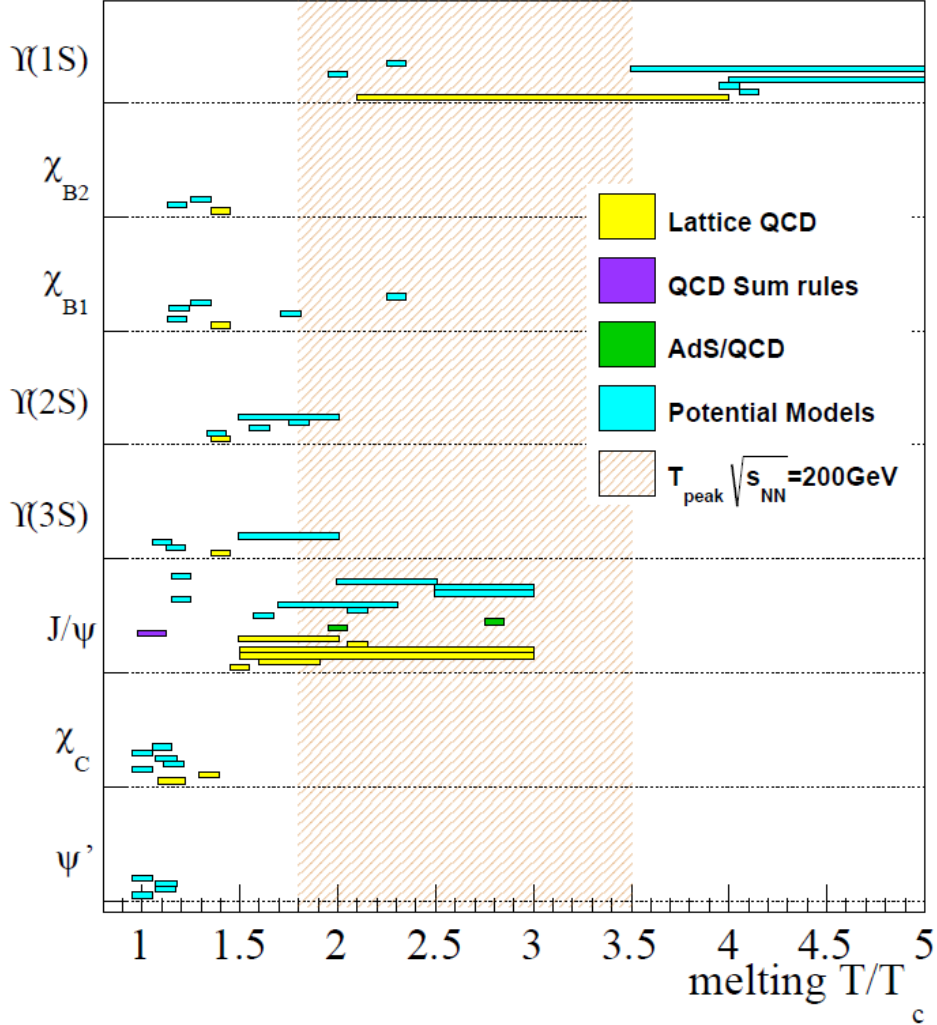


Fig. 2.3: Ratios of the quarkonium melting temperature T and the QGP critical temperature T_C calculated by a variety of models: Lattice QCD, QCD sum rules, AdS/QCD, potential models. The shaded band denotes the estimation for the peak temperature in Au+Au collisions of $\sqrt{s_{NN}} = 200$ GeV at RHIC [10].

Nonetheless, these secondarily produced quarkonia differ in kinematic distributions. Namely, their average p_T would be smaller. This makes them distinguishable from the primarily produced ones, especially if the quarks come from quarkonia melting [6].

2.3.2.2 Cold nuclear matter effects

Cold nuclear matter (CNM) effects include all phenomena influencing the quarkonia production which do not arise from the presence of QGP and do not occur in proton-proton collisions. They are the consequences of the different behaviour of partons in heavy nucleus than in single proton.

Some of these are:

- **Nuclear shadowing** - comes from the fact that parton distribution functions (PDF), which are the momentum distributions of the partonic content of a nucleon, change when the nucleon is inside a nucleus. This, subsequently, causes a change in the $Q\bar{Q}$ pair production. This change can be suppressing as well as enhancing (antishadowing) [11].
- **Cronin effect** - accounts for the initial state energy loss of the partons, caused by the multiple scattering of proton's partons off the nucleus' partons. This modifies partons', and then the produced $Q\bar{Q}$ pairs' momenta [12].
- **Nuclear absorption** - describes the final state interaction of the $Q\bar{Q}$ with the nucleonic remnants of the heavy ion. This can modify, or even destroy, the state [13].
- **Co-mover absorption** - is the interaction of the pre-quarkonium $Q\bar{Q}$ state with other mesons created in the collision [6].

2.4 Decay channels and feed-down

Most common decay modes of the quarkonia states can be found in Fig. 2.1. Detailed overview of decay channels of biggest interest is shown in Tab. 2.2. It includes information

2.4. DECAY CHANNELS AND FEED-DOWN

| Quarkonium | Mass [GeV] | Width [keV] | Decay channel | BR |
|----------------|------------|-------------|--------------------------------|-------------------|
| J/ψ | 3.097 | 92.9 | \rightarrow hadrons | 87.7 |
| | | | $\rightarrow e^+e^-$ | 6.0 |
| | | | $\rightarrow \mu^+\mu^-$ | 6.0 |
| $\psi(2S)$ | 3.686 | 298 | $\rightarrow J/\psi + X$ | 61.0 |
| | | | $\rightarrow e^+e^-$ | $8 \cdot 10^{-3}$ |
| $\Upsilon(1S)$ | 9.460 | 54.0 | \rightarrow hadrons | 86.9 |
| | | | $\rightarrow e^+e^-$ | 2.4 |
| | | | $\rightarrow \mu^+\mu^-$ | 2.5 |
| $\Upsilon(2S)$ | 10.023 | 32.0 | $\rightarrow \Upsilon(1S) + X$ | 26.5 |
| | | | $\rightarrow e^+e^-$ | 1.9 |
| | | | $\rightarrow \mu^+\mu^-$ | 1.9 |
| $\Upsilon(3S)$ | 10.036 | 20.3 | $\rightarrow \Upsilon(2S) + X$ | 10.6 |
| | | | $\rightarrow \Upsilon(1S) + X$ | 6.6 |
| | | | $\rightarrow \mu^+\mu^-$ | 2.2 |

Tab. 2.2: Interesting decay channels of significant quarkonia. The branching ratio BR is presented for each decay mode. Quarkonia states mass and width are also shown. Values taken from [5].

about the state mass, width, mode of decay and its branching ratio. The width, also noted as Γ is inversely proportional to the particle lifetime and correlates to the detected signal peak width. The branching ratio BR gives the percentual probability of the state to decay in said channel.

It is crucial to notice that the ground states J/ψ and $\Upsilon(1S)$ can be decayed to from the excited states. Such production is called non-prompt or *feed-down*. Apart from the listed hadronic decays of the excited states, there are also radiative decays of χ_c or χ_b and weak decays of heavier quarks contributing to this secondary non-prompt production. Together, as much as 50% of the produced J/ψ or $\Upsilon(1S)$ can be caused by the feed-down. Accordingly, this must be taken into account. For instance, if we observe a 60% suppression of the $\Upsilon(1S)$ signal, it could be that no ground state created in the initial stages of the collision were suppressed and the apparent decline is caused by the suppression of $\Upsilon(2S)$ and $\Upsilon(3S)$ [14].

Chapter 3

Recent results in Υ studies

In this chapter, some of the important recent results on Υ quarkonia are presented. Shown analyses were conducted at the world's leading particle accelerators — the LHC and the RHIC. The average number of heavy quark pairs produced at these accelerators is compared in Tab. 3.1.

3.1 LHC

At LHC, the Υ is studied to extent at all of its major experiments. Its production in Pb+Pb collisions was studied at ALICE and CMS. These results as well as results from p+Pb collisions at ATLAS and ALICE are presented.

| Event at | RHIC 200 GeV | LHC 2.76 TeV |
|-----------------------------|--------------|--------------|
| $N_{c\bar{c}}/\text{event}$ | 13 | 115 |
| $N_{b\bar{b}}/\text{event}$ | 0.1 | 3 |

Tab. 3.1: Estimated number of heavy $Q\bar{Q}$ pairs created per central collision event (0-10%) at RHIC and LHC energies [15].

3.1. LHC

3.1.1 ALICE

The ALICE experiment is LHC's main heavy ion collisions detector. Its researchers have brought results on Υ measurements in Pb+Pb, p+Pb, and p+p collisions. Due to the experiment's nature, the measurements using the dimuon decay channel have been done at forward rapidity ($2.5 < y < 4$).

3.1.1.1 Pb+Pb collisions

The suppression of $\Upsilon(1S)$ at forward rapidity in Pb+Pb collisions at $\sqrt{s_{NN}} = 2.76$ TeV and down to zero transverse momentum p_T was studied in 2014, using the dimuon decay channel [16].

First, the candidates of muon tracks were reconstructed, beginning at the hits in tracking chambers. Trigger and vertices conditions were applied onto the data as well as track quality and physics cuts.

The $\Upsilon(1S)$ raw yield was acquired from the fit of the dimuon invariant mass distribution. These were found for different centrality and rapidity windows and are shown in Fig. 3.1. The Υ peaks were fit by Crystal Ball functions, whereas sum of two exponentials was used for the background.

The raw yield $N[\Upsilon(1S)]$ was further adjusted to account for the detector acceptance and efficiency ($A \times \varepsilon$), the branching ratio of the dimuon decay $\text{BR}_{\Upsilon(1S) \rightarrow \mu^+ \mu^-}$, and appropriately normalised to the total number of minimum bias events N_{MB} . Doing so, the yield $Y_{\Upsilon(1S)}$ was acquired via

$$Y_{\Upsilon(1S)} = \frac{N[\Upsilon(1S)]}{(A \times \varepsilon) \times \text{BR}_{\Upsilon(1S) \rightarrow \mu^+ \mu^-} \times N_{\text{MB}}} . \quad (3.1)$$

To quantify the effects of the nuclear medium on the production, a nuclear modification factor is used, defined as follows,

$$R_{\text{AA}} = \frac{Y_{\Upsilon(1S)}}{\langle T_{\text{AA}} \rangle \times \sigma_{\Upsilon(1S)}^{\text{pp}}} \quad (3.2)$$

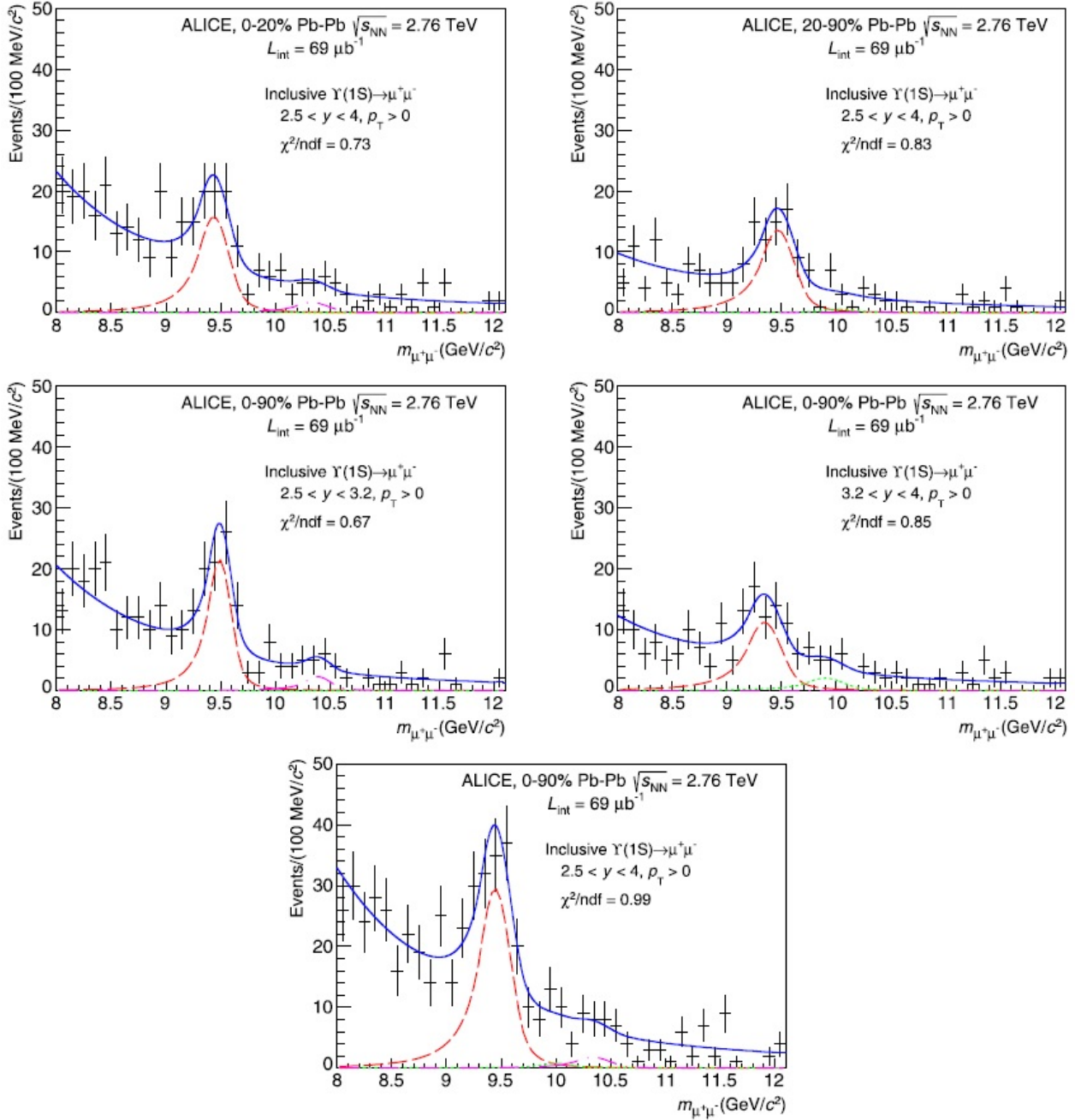


Fig. 3.1: Distribution of invariant mass of unlike sign dimuons with $p_T > 0$ in different centrality and rapidity regions in Pb+Pb collisions. Red, green, and magenta lines represent the $\Upsilon(1S)$, $\Upsilon(2S)$, and $\Upsilon(3S)$ peaks, respectively. The blue solid line represents the total fit including background. Measured at ALICE [16].

3.1. LHC

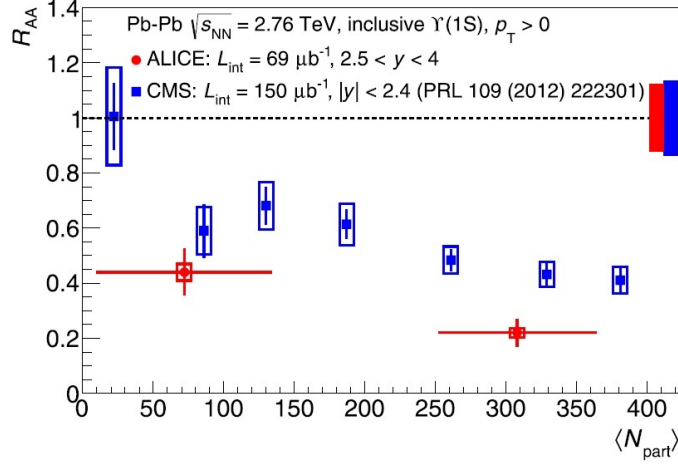


Fig. 3.2: Results of R_{AA} of inclusive $\Upsilon(1S)$ in Pb+Pb collisions as a function of mean number of participants $\langle N_{part} \rangle$. Shown ALICE data at $2.5 < y < 4$ are compared with CMS data [17] at $|y| < 2.4$ [16].

where $\langle T_{AA} \rangle$ is a quantity interpretable as the normalised average number of nucleon-nucleon binary collisions (which is proportional to the number of participants $\langle N_{part} \rangle$ and is centrality dependent) and $\sigma_{\Upsilon(1S)}^{pp}$ is the cross section in p+p collisions at same energy. $\langle T_{AA} \rangle$ was calculated by the means of Glauber model and $\sigma_{\Upsilon(1S)}^{pp}$ was gained by the interpolation of LHCb data to adequate rapidity regions, since it had been insufficiently measured at ALICE.

Obtained results of R_{AA} with uncertainties as functions of participant nucleons $\langle N_{part} \rangle$ and rapidity y are shown in Fig. 3.2 and Fig. 3.3, respectively. A comparison with calculations from theoretical models (in the latter) and with the data from CMS (in both figures) is also displayed [17].

The results of R_{AA} show that the suppression of $\Upsilon(1S)$ is greater in central (0-20%) than in semi-peripheral (20-90%) collisions. Combined with the CMS data, they also exhibit rapidity dependence. The observed suppression is stronger than the considered theoretical models predict. The trend in rapidity is also opposite to the one calculated by dynamical models. A better knowledge of CNM effects and accurate measurements on $\Upsilon(1S)$ feed-down from heavier bottomonia are needed in order to draw rigorous conclusions [16].

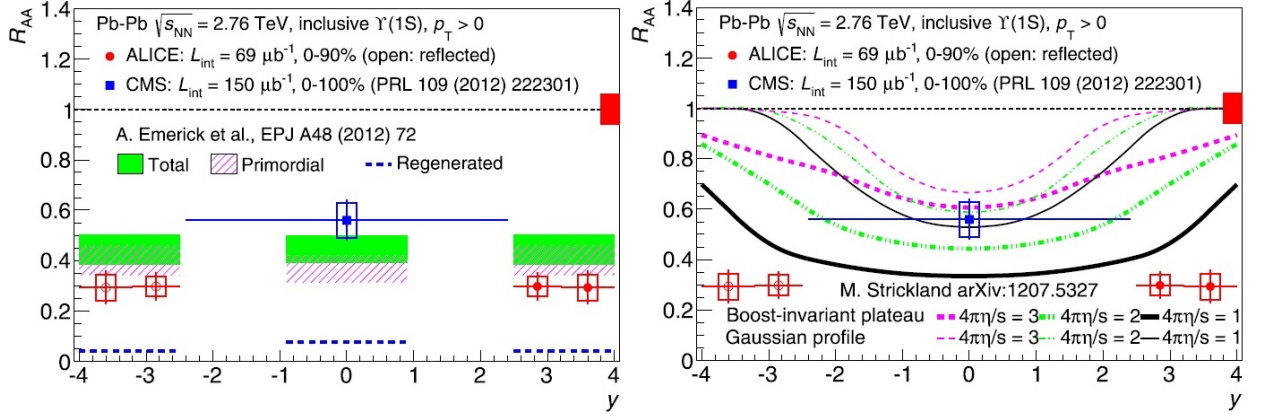


Fig. 3.3: Results of R_{AA} of inclusive $\Upsilon(1S)$ in Pb+Pb collisions as a function of rapidity y . CMS data [17] are also shown. The results are compared with calculations from a transport (left) and dynamical (right) model [16].

3.1.1.2 p+Pb collisions

The production of $\Upsilon(1S)$ and $\Upsilon(2S)$ in p+Pb at $\sqrt{s_{NN}} = 5.02$ at forward and backward rapidity intervals and down to zero transverse momentum via the dimuon decay channel in 2014 [18].

Since the p and Pb beams have different charge to mass ratio, they also differ in energies ($E_p = 4$ TeV and $E_{Pb}/A_{Pb} = 1.58$ TeV). Thus, the centre-of-mass system (CMS) of the collisions is moved in rapidity by $\Delta y = 0.465$ with respect to the laboratory frame in the direction of the p beam (i.e. $y_{cms} = y_{lab} - \Delta y$).

The ALICE experiment is able to measure muons via its spectrometer in the laboratory rapidity interval of $2.5 < y_{lab} < 4$. Taking into account said shift, the measurements were taken in the backward region of $-4.46 < y_{cms} < -2.96$, with the p beam travelling opposite to the direction of the spectrometer, or in the forward region of $2.03 < y_{cms} < 3.53$, alternatively. The positive y region is defined by the direction of the p beam. As such, the data had to be combined from two beam configurations.

To reach results, the data were reconstructed and worked on similarly to the case of Pb+Pb measurements. The raw yield signals of Υ states were extracted from the unlike-sign

3.1. LHC

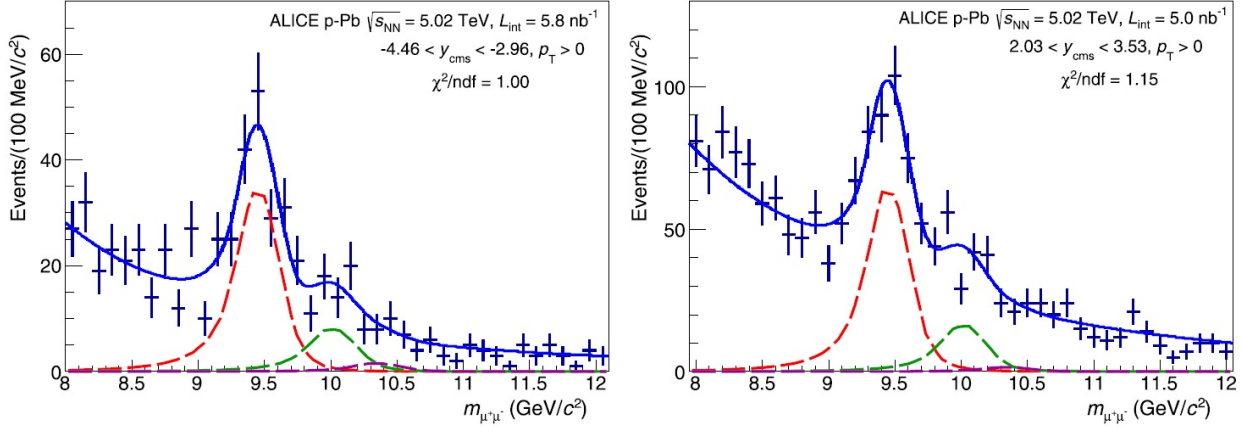


Fig. 3.4: Distribution of invariant mass of unlike-sign dimuons with $p_T > 0$ in forward and backward rapidity regions in p+Pb collisions. The red, green, and purple dashed lines represent the three Υ states. The blue solid line represents the total fit including background. Measured at ALICE [18].

dimuon invariant mass distribution, which is shown in Fig. 3.4 for both rapidity windows. Additionally, the $\Upsilon(2S)$ peak appeared to be significant enough to allow reliable measurements.

The nuclear modification factor in p+Pb collisions R_{pPb} was calculated as

$$R_{pPb} = \frac{\sigma_{\Upsilon(nS)}^{pPb}}{A_{Pb} \times \sigma_{\Upsilon(nS)}^{pp}}, \quad (3.3)$$

where $\sigma_{\Upsilon(nS)}^{pPb}$ is the cross section gained equivalently to the normalised yield Y in the Pb+Pb measurements, $A_{Pb} = 208$ is the mass number of lead [18] and $\sigma_{\Upsilon(nS)}^{pp}$ is the cross section in p+p collisions at $\sqrt{s} = 5.02$ TeV. Since the last had not been measured, interpolation in \sqrt{s} of data from LHCb was utilised.

Calculated results of R_{pPb} with uncertainties for $\Upsilon(1S)$ as a function of rapidity are displayed in Fig. 3.5. For comparison, values of the quantity calculated by various models are also shown.

At forward rapidity, the results in p+Pb collisions exhibit suppression with respect to p+p collisions. The suppression is not observed at backward rapidity. This is also inconsistent

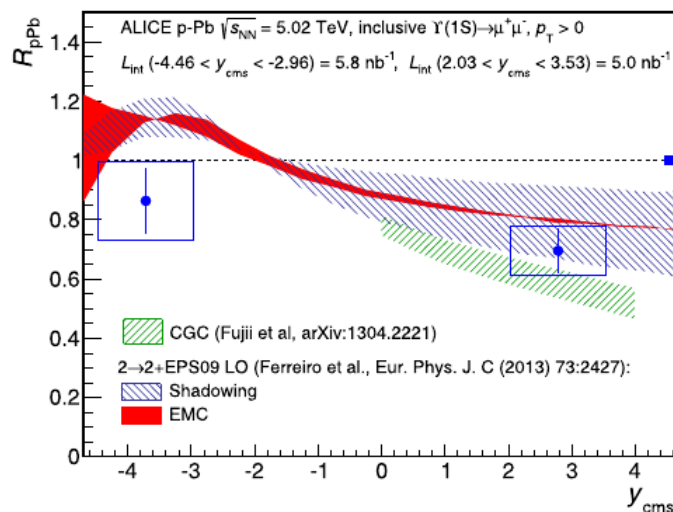


Fig. 3.5: Results of R_{pPb} of inclusive $\Upsilon(1S)$ in p+Pb collisions as a function of rapidity. Model calculations are also displayed. Measured at ALICE [18].

with calculations from models, which predict slight enhancement in the interval. At forward rapidity, the data is in agreement with the calculations.

Moreover, the $[\Upsilon(2S)/\Upsilon(1S)]_{pPb}$ quantity was calculated in both forward and backward rapidity windows. This is a ratio of the measured cross sections of $\Upsilon(2S)$ and $\Upsilon(1S)$ in p+Pb collisions. At both rapidity regions, the ratios are mutually consistent. Furthermore, they are within uncertainties in accord with the ratio measured in p+p collisions at LHCb. This indicates uniformity of CNM influence on the two states [18].

The results suffer from large uncertainties. Therefore, more accurate measurements with richer statistics are needed before altering the models and quantifying the CNM behaviour in Pb+Pb collisions in an appropriate manner.

3.1.2 ATLAS

ATLAS is LHC's biggest experiment and its core objective is to discover new physics, mainly in p+p collisions. However, a heavy ion programme exists within this multi-purpose detector research. ATLAS team have come up with results on Υ in p+Pb collisions. Nevertheless, to this date no results on Υ in Pb+Pb have been published.

3.1. LHC

3.1.2.1 p+Pb collisions

Measurements of the Υ family production in p+Pb collisions at $\sqrt{s_{\text{NN}}} = 5.02$ TeV were carried out in 2015, using the data gathered in 2013 [19].

Identically to the case of ALICE, due to the asymmetry in beam energies, a shift in rapidity for the CMS occurs. The shifted rapidity is this time denoted as y^* and is defined to be positive in the p beam direction.

The muon candidates were reconstructed by combining tracks of charged particles rebuilt in inner detector and muon spectrometer. Constraints on vertex origin, track quality, and rapidity ($-2.25 < y^* < 1.2$) were applied.

The differential cross section $\frac{d^2\sigma_{\Upsilon(\text{nS})}}{dp_T dy}$ was computed in accordance with

$$\frac{d^2\sigma_{\Upsilon(\text{nS})}}{dp_T dy} \times \text{BR}_{\Upsilon(\text{nS}) \rightarrow \mu^+ \mu^-} = \frac{N_{\Upsilon(\text{nS})}}{\Delta p_T \times \Delta y \times \int \mathcal{L} dt}, \quad (3.4)$$

where $\text{BR}_{\Upsilon(\text{nS}) \rightarrow \mu^+ \mu^-}$ is the branching ratio, $N_{\Upsilon(\text{nS})}$ the number of produced Upsilon's, Δp_T and Δy the widths of corresponding intervals, and $\int \mathcal{L} dt$ the integrated luminosity.

$N_{\Upsilon(\text{nS})}$ was acquired by applying the corrections for detector acceptance and efficiency to the raw yield extracted from fit of invariant mass spectrum. This is displayed in Fig. 3.6. Same distribution, in rapidity window $|y| < 2.25$, was also measured for p+p collision and is shown in the same figure for comparison. A weighted sum of Gaussian and Crystal Ball functions was used to fit the bottomonia states yields. A combination of an exponential and second order polynomial functions was used to describe the background.

Nuclear modification factor was calculated as follows,

$$R_{\text{pPb}} = \frac{1}{A^{Pb}} \frac{d^2\sigma^{\text{pPb}}/dy dp_T}{d^2\sigma^{\text{pp}}/dy dp_T}. \quad (3.5)$$

The value of cross section for $p+p$ collisions at $\sqrt{s} = 5.02$ TeV was obtained by interpolating the results for said cross section at $\sqrt{s} = 2.76$ TeV and $\sqrt{s} = 7$ TeV. The results of R_{pPb} as a function of y^* are shown in Fig. 3.7 along with LHCb and ALICE results.

In conclusion, the results show no pronounced rapidity dependence in mid-rapidity region.

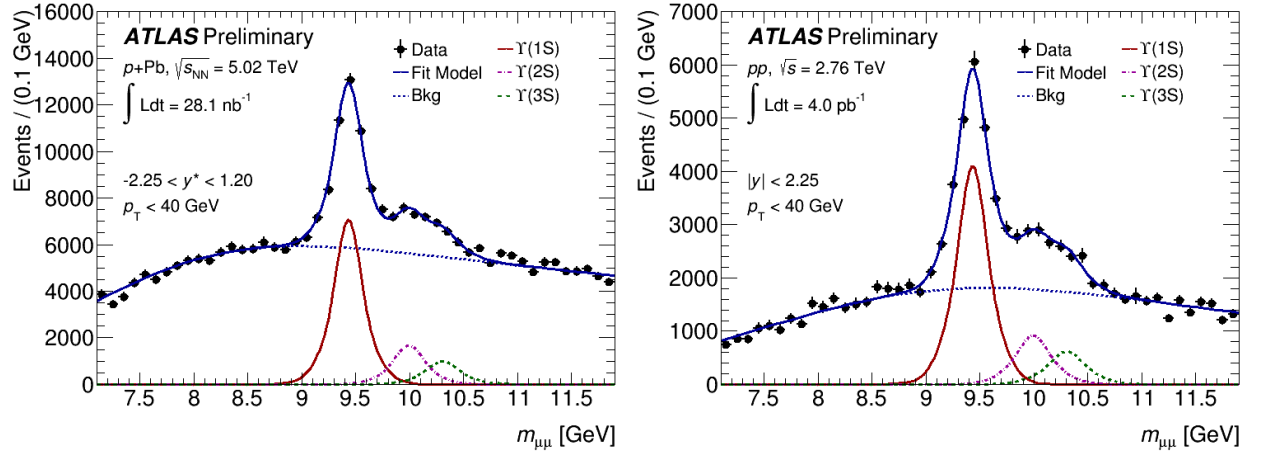


Fig. 3.6: Distributions of invariant mass of unlike-sign dimuons in p+Pb collisions with $-2.25 < y^* < 1.20$ (left) and p+p collisions with $|y| < 2.25$ (right); with acceptance correction applied. Red, purple, and green lines represent the fits of three Υ states. Dotted blue line represents the background and solid blue line is the total fit. Measured at ATLAS [19].

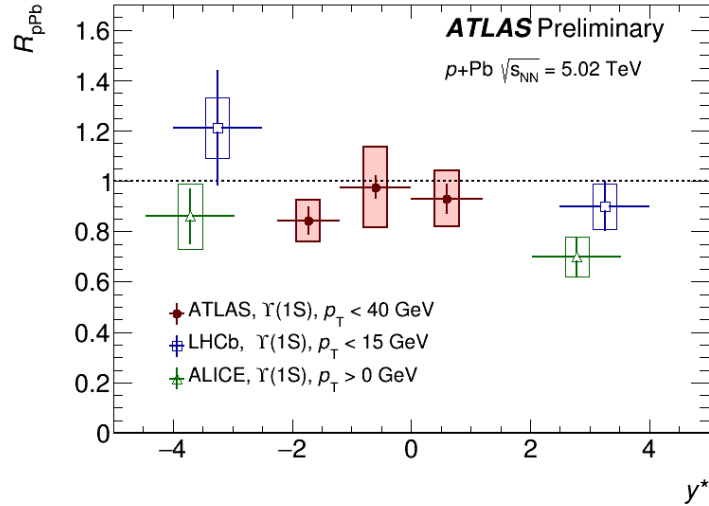


Fig. 3.7: Results of nuclear modification factor R_{pPb} for $\Upsilon(1S)$ as a function of y^* in p+Pb collisions at $\sqrt{s_{NN}} = 5.02$ TeV. Results from LHCb and ALICE are also shown. Measured at ATLAS [19].

3.1. LHC

In said analysis, centrality dependence of R_{pPb} was also tested, using Glauber and GGCF models. That being said, the factor is observed to be almost constant in $\langle N_{\text{part}} \rangle$. The ratios of excited to ground states were calculated as well, both in p+Pb and p+p collisions. Again, they exhibit no obvious dependence on p_T nor y . This ratio, however, is found to be relatively bigger in peripheral and relatively smaller in central p+Pb collisions than same ratios in p+p collisions [19].

3.1.3 CMS

The CMS is another general purpose detector at LHC. Its fields of study are similar to ATLAS. After ALICE, the CMS has the strongest HIP programme at LHC. Measurements of Υ production in p+p, Pb+Pb, and p+Pb have been carried out [17].

Analyses of the first two kinds of collisions were presented in 2012, using the data collected in 2011, with the collision energy $\sqrt{s_{\text{NN}}} = \sqrt{s} = 2.76$ TeV. The tracks were identified via the combination of silicon inner tracker and muon spectrometers, with selection threshold applied on muon momenta and rapidities. Resulting invariant mass spectra for p+p and Pb+Pb collisions can be found in Fig. 3.8. They share the reconstruction algorithm.

The nuclear modification factor R_{AA} was calculated as follows,

$$R_{\text{AA}} = \frac{\mathcal{L}_{\text{pp}}}{T_{\text{AA}} N_{\text{MB}}} \frac{\Upsilon(nS)|_{\text{PbPb}}}{\Upsilon(nS)|_{\text{pp}}} \frac{\varepsilon_{\text{pp}}}{\varepsilon_{\text{PbPb}}}, \quad (3.6)$$

where $\Upsilon(nS)$ are the total yields for given state, ε the correcting efficiencies, \mathcal{L} and N_{MB} the integrated luminosity and number of minimum bias events resp. (to account for normalisation), and T_{AA} the nuclear overlap function, which is interpretable as the average number of binary collisions. The following R_{AA} results were found:

1. $R_{\text{AA}}(1S) = 0.56 \pm 0.08(\text{stat.}) \pm 0.07(\text{syst.})$,
2. $R_{\text{AA}}(2S) = 0.12 \pm 0.04(\text{stat.}) \pm 0.02(\text{syst.})$,
3. $R_{\text{AA}}(3S) = 0.03 \pm 0.084(\text{stat.}) \pm 0.01(\text{syst.})$.

The division in centrality regions was also studied for the ground state as well as for the

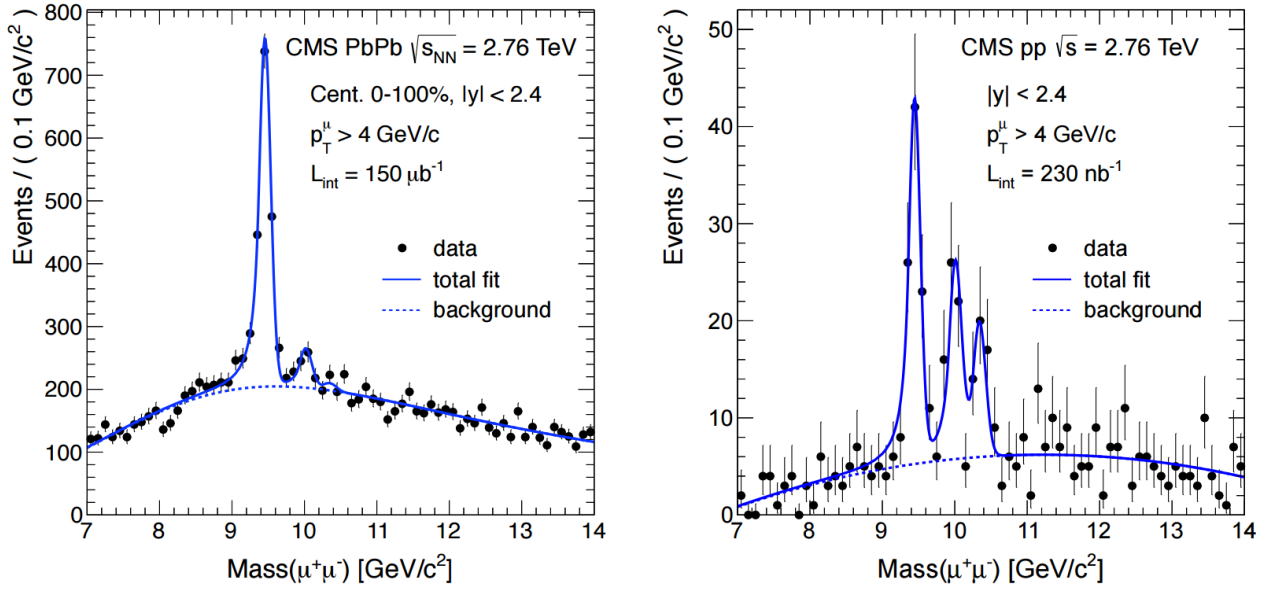


Fig. 3.8: Distribution of invariant mass of unlike-sign dimuons in Pb+Pb collisions (left) and p+p collisions (right) of $\sqrt{s_{NN}} = \sqrt{s} = 2.76$ TeV with cuts on $|y| < 2.4$ and $p_T > 4$ GeV. The dotted lines denote the background fits and the solid one the total signal. Measured at CMS [17].

3.2. RHIC

$\Upsilon(2S)$ excited state. The results show clear decrease of R_{AA} in $\langle N_{\text{part}} \rangle$, indicating a weaker suppression in peripheral events. They can be found in Fig. 5.7 in Chapter 5 of this thesis.

3.2 RHIC

The RHIC — *Relativistic Heavy Ion Collider* — is an accelerator located at Brookhaven National Laboratory in New York, USA. RHIC is where the QGP discovery was first announced. The STAR and PHENIX experiments have always been of big importance in the field of heavy ion collision studies. At RHIC, collisions of many kinds of ions are looked at. The Υ was studied in Au+Au, d+Au, and also at U+U collisions.

3.2.1 STAR and PHENIX

The STAR detector (Solenoidal Tracker at RHIC) is RHIC's key experiment in the studies of QGP. It was mainly designed to measure hadronic observables and flow signatures of nuclear medium. As such, it operates at mid-rapidity. Studies of heavy quarkonia have been carried out, mainly via the dielectron decay channel at $|y| < 1$. Nonetheless, after recent upgrades, the dimuon decay is also utilised and measured at $|y| < 0.5$ [20].

The instalment of Muon Telescope Detector (MTD) was a principal part of the upgrade. It is capable of triggering on muons as well as identifying them. It is expected to allow measurement of separated Υ states for the first time at STAR [20].

Measurements on Υ production via muons have been ongoing and first results for Au+Au collisions at $\sqrt{s_{NN}} = 200$ GeV, using only 30% of acquired statistics, were published in 2015. Muon candidates were reconstructed by combination of Time Projection Chamber (TPC), STAR's main tracking device, and MTD. Computed invariant mass distribution of dimuons can be seen in Fig. 3.9. Notably, it lags behind LHC's results in statistics, nonetheless, they are expected to improve by the factor of 6 by the end of the year [20].

Analysis on Υ suppression using the dielectron decay channel in Au+Au and d+Au collisions at $\sqrt{s_{NN}} = 200$ GeV was published in 2013 by the STAR team. TPC along with

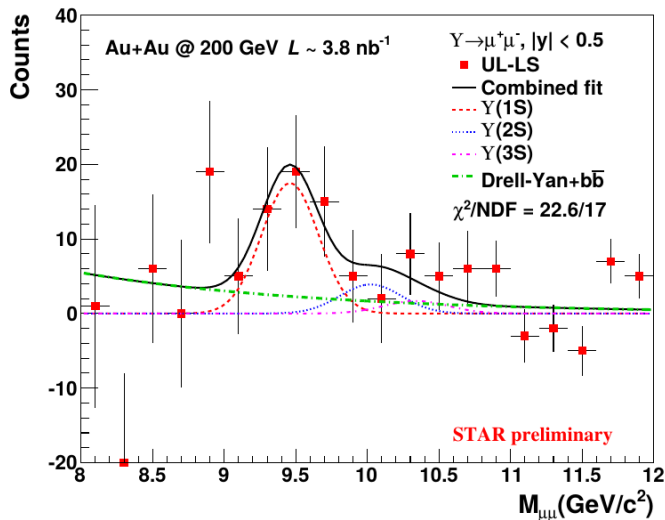


Fig. 3.9: Invariant mass distributions of unlike-signed dimuons in Au+Au collisions at $\sqrt{s_{\text{NN}}} = 200$ GeV at $|y| < 0.5$. The red, blue, and magenta lines represent the fit shapes of Υ states. The green line represents background events, estimated by PYTHIA. Black line represents the total fit. Measured at STAR [20].

electromagnetic calorimeters were used for triggering and electron reconstructions [21].

Found invariant mass distributions of dielectrons for Au+Au (at selected centrality window) and d+Au collisions are both shown in Fig. 3.10. The low significance of different Υ states does not allow for rigorous measurement of separate yields.

Calculated nuclear modification factors R_{AA} and R_{dAu} as functions of $\langle N_{\text{part}} \rangle$ (both) and y (only R_{dAu}) can be found in Fig. 3.11. A comparison with model calculations is also included. A richer statistics is required to draw relevant conclusions, however, a stronger suppression of inclusive Υ in Au+Au than in d+Au is observed.

PHENIX (Pioneering High Energy Nuclear Interaction eXperiment) is another important detector at RHIC. It was designed to measure direct probes of the collisions, that is particles which do not interact strongly in the medium, i.e. photons, electrons, and muons. It enriches STAR studies of Υ by providing results in further rapidities ($1.2 < y < 2.2$). Results of R_{dAu} are displayed along with STAR data again in Fig. 3.11.

3.2. RHIC

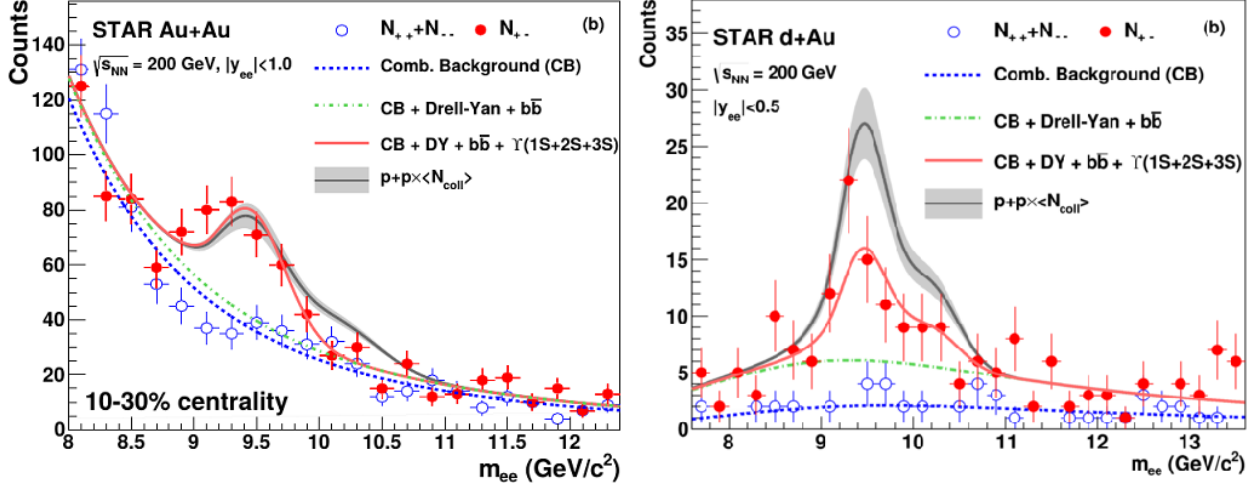


Fig. 3.10: Invariant mass distributions of unliked-sign (red) and like-sign (blue) di-electrons in Au+Au collisions in selected centrality window (left) and d+Au collisions (right) at $\sqrt{s_{NN}} = 200$ GeV. The red line represents the total fit of Υ mesons and estimated background. The black line with grey errorbands show matching yield in p+p collisions, adequately scaled. Measured at STAR [21].

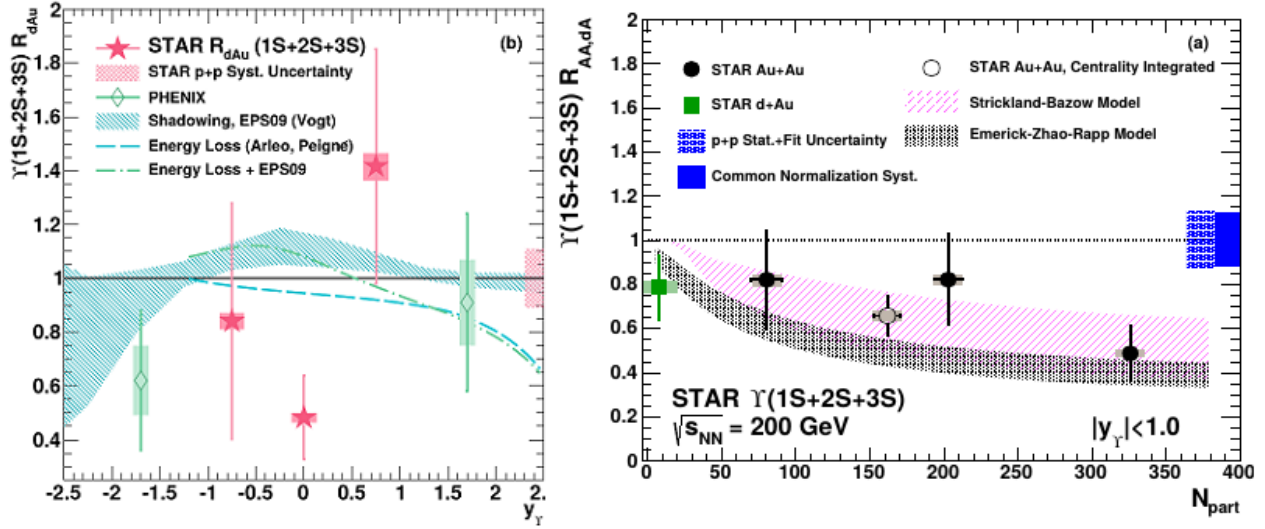


Fig. 3.11: Results of R_{dAu} as a function of rapidity (left) and results of R_{dAu} and R_{AA} as a function of average number of participants (right). Star symbols represent the data from STAR, whereas diamond symbols depict results from PHENIX. Calculations from models are shown in both for comparison [21].

Chapter 4

ATLAS experiment

One of the aspects responsible for particle physics being such a singular field is the sheer fact that it is so difficult and challenging to experimentally test. Unlike other sciences wherein one can utilise various microscopes — or even own senses — to spectate processes, this comes out of question in particle physics. The reason for this is because its objects of study occupy volumes of few cubic femtometers and its interactions often happen in fractions of seconds.

Thus, a probe must have very fine resolution, in order to 'see' said objects. This is achieved by increasing the probe's energy.¹ Furthermore, many of the particles or phenomena come into observable existence only under extreme conditions. For these two reasons, apart from others, a complex facility capable of accelerating particles to very high energies is needed.

4.1 Large Hadron Collider

With its circumference of 27 km and beam energy of 7 TeV, the Large Hadron Collider (LHC) is currently the largest, most powerful, and — arguably — the most important accelerator in the world. It is a principal part of the European Council for Nuclear Research (CERN) accelerator complex and is situated near Geneva, on the border of Switzerland and France.

Various fields of research are studied at CERN laboratories. The main focus is set on

¹Simply said, this is decreasing the probe 'size' according to the De Broglie's relation $\lambda = \frac{h}{E}$.

4.1. LARGE HADRON COLLIDER

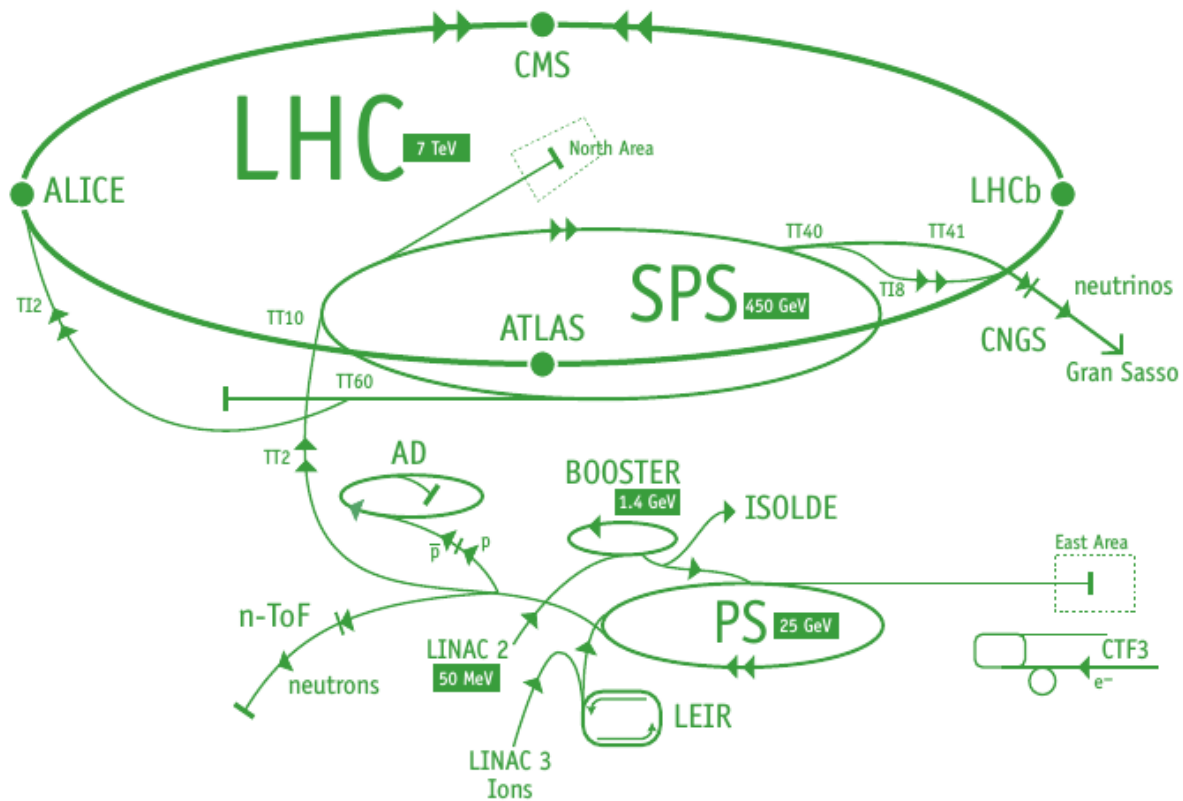


Fig. 4.1: Diagram of the entire CERN accelerator complex showing beam paths, energy acquired at them by a proton, and experimental facilities. Taken from [22].

high energy particle physics, however, its uses in medicine and material sciences are also researched. See the plan of the entire complex in Fig. 4.1.

- **ATLAS** - *A Toroidal LHC ApparatuS* - is LHC's biggest experiment and is a general purpose detector. As such, its design allows to research very wide areas of physics. These include: experimental scrutiny of the Standard Model, search for new particles and extra dimensions, supersymmetry (SUSY).
- **ALICE** - *A Large Ion Collider Experiment* - is LHC's primary experiment for the analysis of lead ions collisions. Its goals are to study the collective behaviour of nuclear matter, create the QGP and evaluate its properties.
- **CMS** - *Compact Muon Solenoid* - shares ATLAS' physics goals, however, differs in

technical design. Its purpose is to strengthen the credence of ATLAS' results and vice versa. Notably, a strong HIP programme is also present.

- **LHCb** - *Large Hadron Collider beauty* - focuses on b -physics (physics of particles containing the b quark) and the behaviour of slight CP violation. It endeavours to answer the absence of antimatter in our universe.

4.2 Experiment's overview

With its cavern the size of half of the Notre Dame Cathedral and its construction weighing over 7000 tonnes of material, ATLAS is by far the CERN's largest experimental facility. Despite being built as a multi-purpose detector, it was designed with a mission in mind - to discover the Higgs boson. Thus, muon spectrometers are ATLAS's most notable feature. ATLAS' design overview is displayed in Fig. 4.2.

Currently, ATLAS' strongest physics programmes are the experimental testing of SM, studies of the b and t quarks, analysis of Higgs boson properties. Others are the search for supersymmetry particles and exotics². A HIP programme is also in operation. Its topics include jet studies, weak bosons production, and heavy quarkonia analysis. The last is also performed in this thesis' final part.

To describe ATLAS's technical setup, one divides it in following sections:

- **Inner Detector (ID)** - also Inner Tracker, is located nearest to the beamline and plays key role in reconstruction of the emitted charged particles' tracks.
- **Calorimeters** - are situated behind the inner detectors and are responsible for the evaluation of particle's energies by stopping them.
- **Muon Spectrometers (MS)** - are the outermost detectors. They identify the properties of muons, the most penetrating particles of our interest, which pass the calorimeters without energy losses.

²These include searches for new forms of matter, extra dimensions, and miniature black holes.

4.2. EXPERIMENT'S OVERVIEW

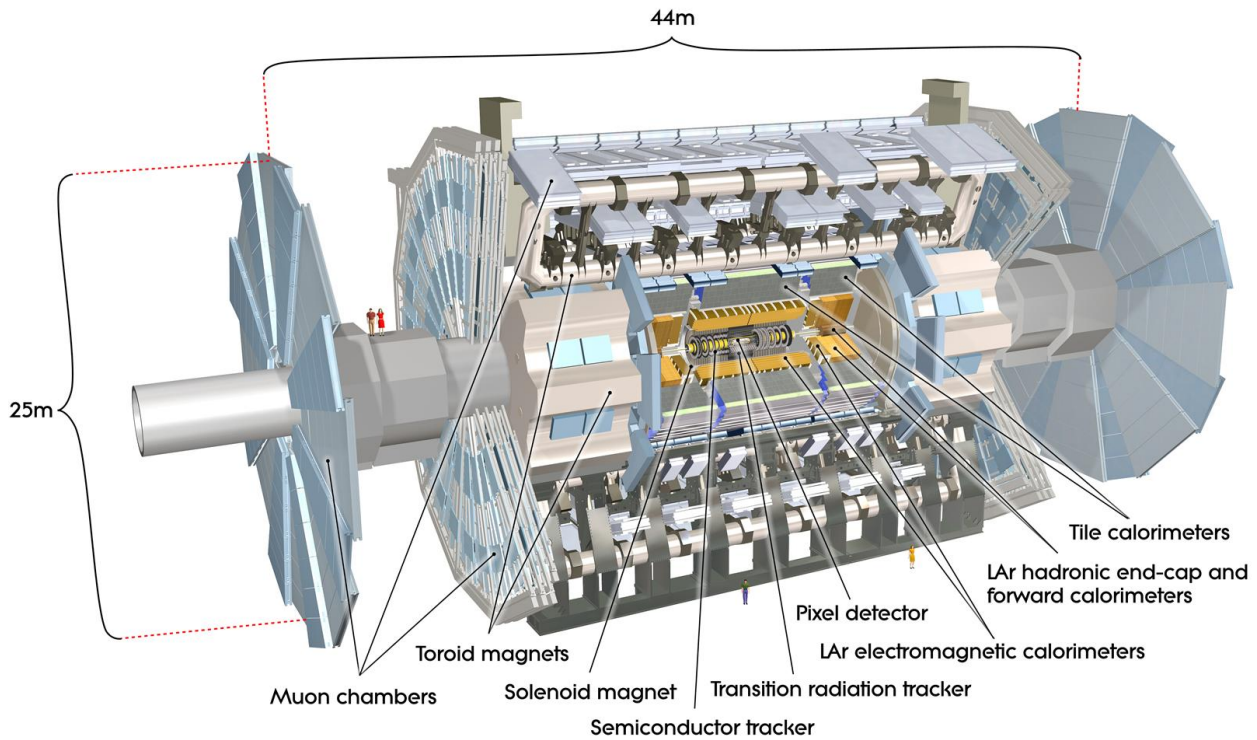


Fig. 4.2: Overview of the ATLAS experiment and its subdetectors and magnets. A size comparison with a standing person can be seen. Taken from [23].

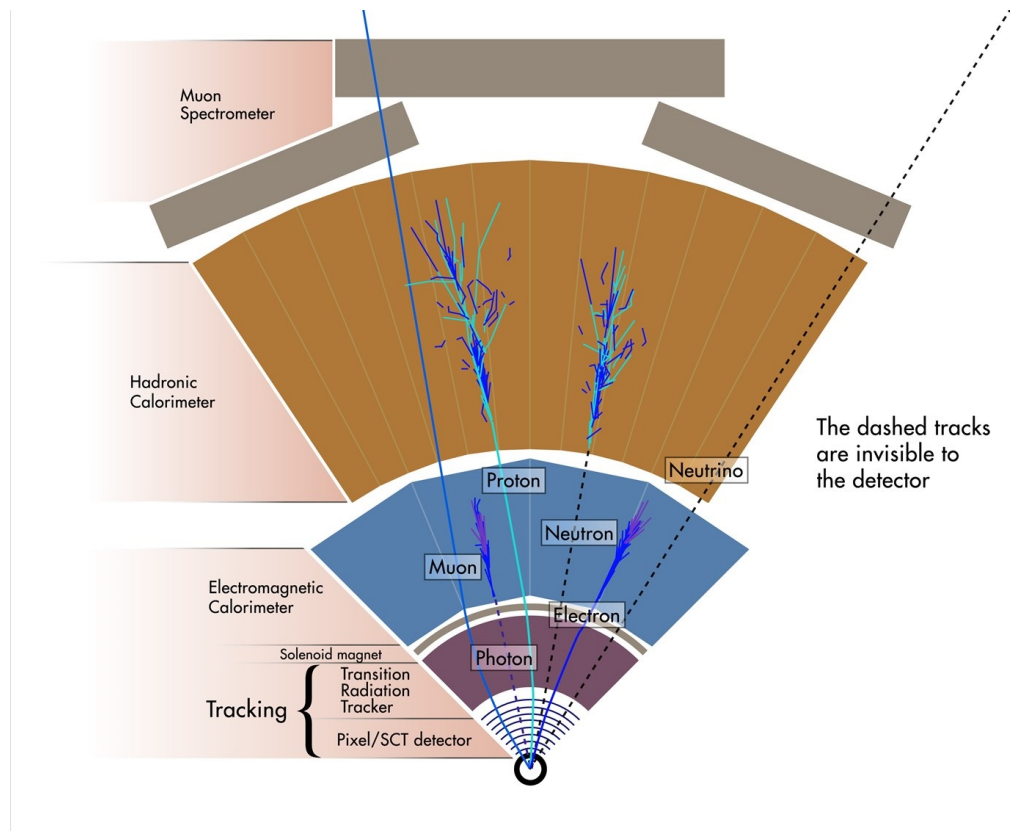


Fig. 4.3: Illustration of how different particles propagate through the layers of the experiment. Taken from [24].

- **Magnet System** - subject the entire detector to strong magnetic fields of ~ 2 T. It bends charged particles' trajectories in accordance with the Lorentz force. The particle's momenta can be then determined from the track curvature.

By the combined utilisation of these, physicists are able to reconstruct the collision event, recognize most produced particles' identities and compute their properties. A concise figure showing how different particles propagate through ATLAS' layers is displayed in Fig. 4.3.

4.3 Inner detector

Inner detector is a principal part of the experiment. It is built of many small 'cells' which can register when a particle passes through them. This is achieved by various physical means. The

4.3. INNER DETECTOR

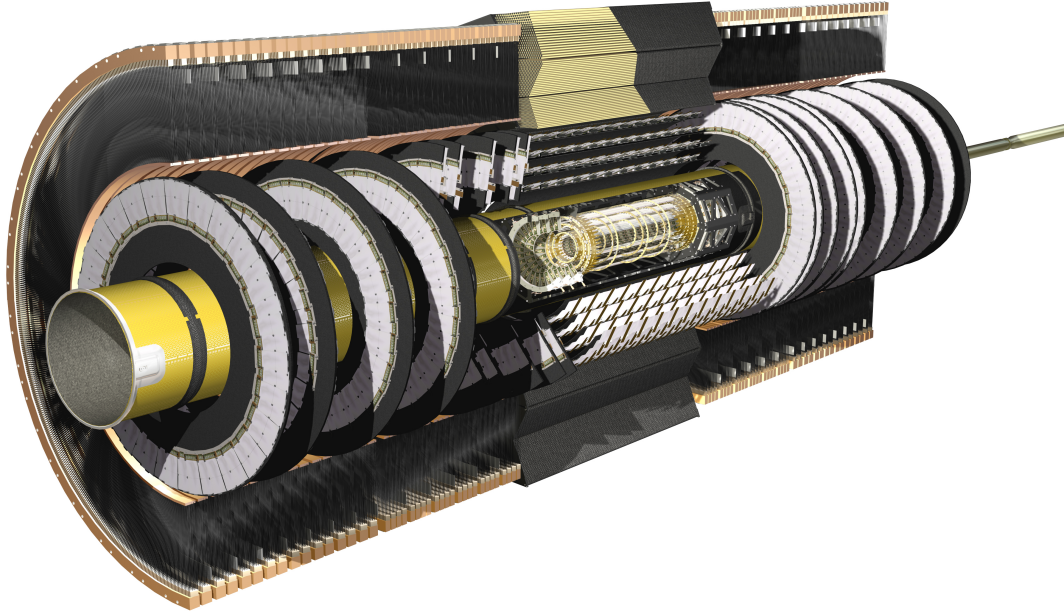


Fig. 4.4: Overview of the ATLAS Inner Detector and its subdetectors. Taken from [25].

resolution (granularity) of these cells is very high, to obtain maximal precision. The crossing points of a particle passing are subsequently used to interpolate particle's trajectory.

ID copies ATLAS' cylindrical design. Hence, it consists of a barrel part and two end-cap parts, to cover good pseudorapidity range. The detector's layout and geometry is illustrated in Fig. 4.4 and Fig. 4.5 [26].

ID is made up of three synergistic sub-detectors:

- **Pixel Detector (PD)** - is the closest to the beampipe and has the biggest granularity. It is built up of many pixels, which serve as the reading units.
- **Semiconductor Tracker (SCT)** - is situated behind the PD. Instead of single pixels, it is made up of many overlaying layers of strips, which together form a lattice.
- **Transition Radiation Tracker (TRT)** - is the outermost sub-detector and also the

largest. It is formed by miniature gaseous chambers (straws) and utilises different physical principle than ID and SCT.

4.3.1 Pixel detector

Function-wise, a pixel detector for particles utilises semi-conductors and is not dissimilar from the sensors in ordinary digital camera. As a charged particle traverses through the silicon material in a pixel, it liberates electrons from the atoms. The electrons (and holes) are then moved by the electric field that the pixel is subjected to. Finally, a signal (current formed by the collected charge) is read out at the pixel's end and evaluated by further electronics.

The PD's basic working unit is a module, which is a ca. 6×2 cm rectangle holding 46,080 pixels. Pixel dimensions are 0.4×0.05 mm. The modules are placed onto staves, which are further arranged in a somewhat turbine pattern into a cylinder. Three concentric cylinders make up the PD, with their axis being the beam. At higher η regions, modules are placed into three concentric discs at each end of said cylinders [26].

In total, there are 67 million pixels in the three cylinders and 13 million pixels in the end-cap discs. To ensure the PD operates at the same rate as the beam collisions (that is 40 MHz), each pixel is equipped with its own independent read-out channel [26].

4.3.2 Semiconductor tracker

The SCT is similar to the PD in principle. However, the module carries silicon strips instead of pixels. These strips have a pitch of 0.08 mm. There are two layers of these strips, one on each side of the module. They are both slightly rotated with respect to each other, to the relative angle of 40 mrad. Like that, they form a grid and can provide information about 2D position of the hit.

There are 4088 modules in the SCT; 2112 of them form 4 concentric cylinders behind the PD and 1976 form 9 concentric end-cap discs on each side at higher η . There are 770 active strip sensor on each side of a module [26].

4.3. INNER DETECTOR

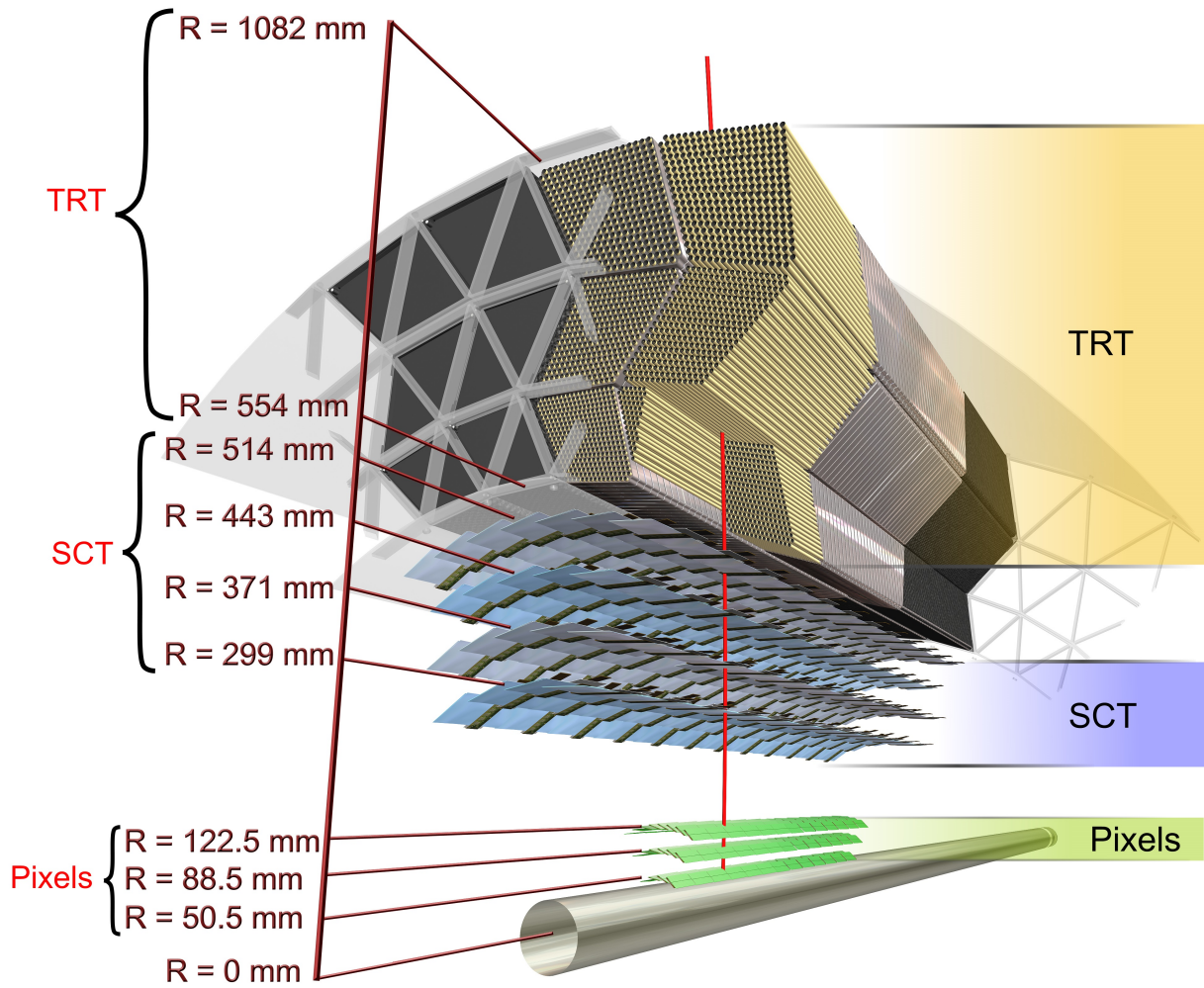


Fig. 4.5: Geometry of the ATLAS Inner Detector. Taken from [25].

4.3.3 Transition radiation tracker

Apart from ionising the semi-conducting silicon, one can also detect a particle by detecting its transition radiation. When a particle crosses a boundary between two media of different refraction index n , the change in the electric field (which is n dependent) is balanced by the emission of photons. Because of the fact that a light particle produces significantly more TR photons than a heavy one, this is particularly effective in detecting electrons.

The TRT consists of a radiator and straw tubes. The radiator is a n -inhomogeneous material which induces the emission of transition radiation photons. The tube straws are small gaseous ionisation cylindrical chambers with a wire in their middle. There is a big electrical potential between the chamber walls and the wire. When photons (induced by the TR in radiator) travel through the gas, they ionise it and liberate electrons. These are then moved by the field to the wire and collected. Hence, a signal is created.

There are 73 layers of straws in the barrel and 160 layered straw planes in the end-caps. Altogether, they hold almost 400,000 straws. Due to the detector's nature, a precise measurement in z cannot be done. Approximately, one expects generation of ~ 36 hits in the detector by a traversing particle [26].

4.4 Calorimeters

The purpose of calorimeters is to measure energy of particles. A calorimeter consists of a stopping material, called also an absorber, and an active detection medium. Whilst losing energy in the absorber, new particles are created. If their energy is sufficiently high, they then produce another. This is called a shower. At ATLAS, there are two sets of calorimeters — an electromagnetic (ECal) and a hadronic (HCal). A schematic of the calorimeters is shown in Fig. 4.6.

4.5. MUON SPECTROMETER

4.4.1 Electromagnetic calorimeter

The ECal is placed directly behind the inner tracker. Its absorber medium are lead plates, folded longitudinally into an accordion pattern and layered side by side in azimuth. In between the plates, there are layers of liquid argon, which serve as the detection medium. Furthermore, read-out electrodes are located in the argon. The ECal consists of a barrel part ($|\eta| < 1.7$) and two end-caps ($1.375 < |\eta| < 3.2$) [26].

For electrons, the main process of losing energy in the absorber is bremsstrahlung, wherein a γ is produced. For photons, the dominant energy loss process is the e^+e^- pair production. The detector has fine granularity and provides sufficiently precise measurement [26].

4.4.2 Hadronic calorimeter

The HCal is located directly behind the ECal. It consists of a central barrel part and a pair of end-caps and forward calorimeters. The forward calorimeter (FCal) covers pseudorapidity of $|\eta| < 4.9$. The barrel is formed by steel absorbers and tile scintillators. These are read-out by wavelength-shifting fibres and photomultipliers. The end-cap parts use liquid argon calorimeters with copper as the absorber. Notably, they are able to detect muons. The FCal also utilises liquid argon, along with the combination of copper and tungsten, to enable electromagnetic calorimetry as well [26].

The hadronic shower created in the absorber is controlled by the strong interaction. The contributing phenomena are: knock-out of nucleons, decay into pions, and nuclear fission.

4.5 Muon spectrometer

The muon detectors are placed at the very end of the detector volume, due to the high penetrativeness of muons. The system consists of four sub-detectors, to reflect the varying requirements of detection and radiation resistance. First, a precise measurement of position is needed. These are provided by the Monitored Drift Tubes (MDT) and the Cathode-strip Chambers (CSC). The second required function is triggering. Such detectors need to give

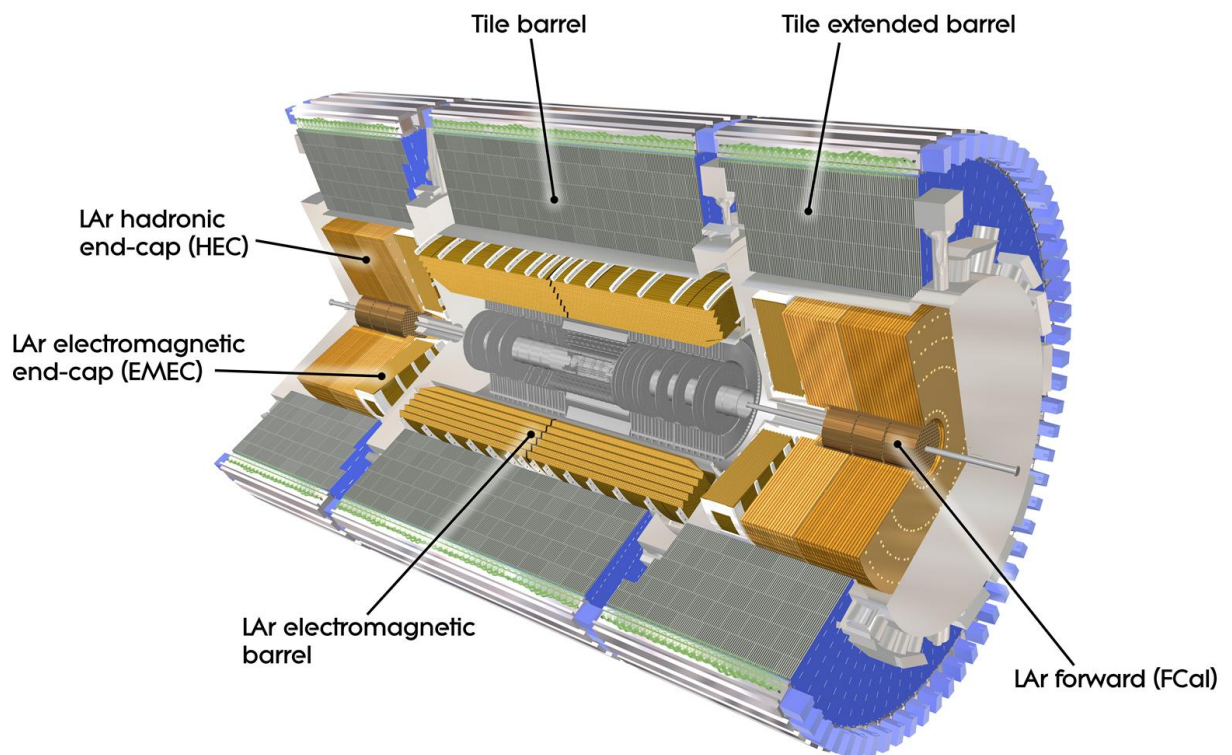


Fig. 4.6: Overview of the calorimeter system at ATLAS. Taken from [27].

4.5. MUON SPECTROMETER

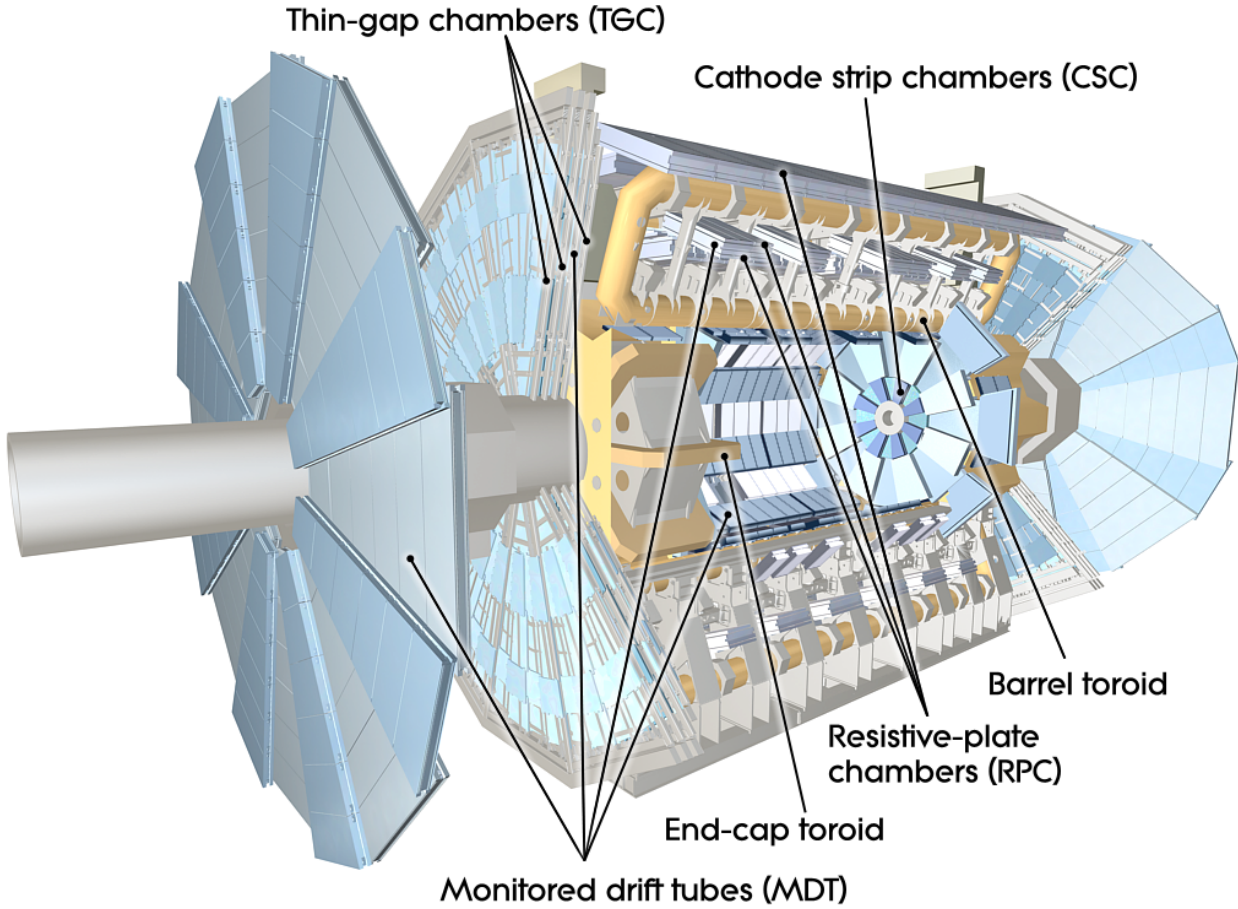


Fig. 4.7: Depiction of the ATLAS muon spectrometer system and subdetectors. Taken from [28].

quick information about the qualitative aspect of the event. These are the Resistive Plate Chambers (RPC) and Thin Gap Chambers (TGC). Layout of the ATLAS muon system is displayed in Fig. 4.7.

4.5.1 Monitored Drift Tubes

The MDTs are the main muon precision measurement detectors at ATLAS. They are built of ~ 30 mm diameter ionisation drift tubes, which are made of aluminium and filled with argon and carbon-dioxide mixture. They cover the pseudorapidity region of $|\eta| < 2.7$, precision of $80 \mu\text{m}$, and very good reliability [26].

4.5.2 Cathode-strip Chambers

The CSCs complement the MDTs' precision measurement in areas where higher counting rates are necessary, that is in $2.0 < |\eta| < 2.7$. It is a multi-wire proportional chamber type of detector and is segmented into strips. A particle's track is then determined by interpolation of the signal in two neighbouring strips. It offers a slightly better granularity than the MDTs [26].

4.5.3 Resistive Plate Chambers

The RPCs are similar to the MDTs in layout, albeit different in purpose. Instead of precision, their priority is detection and read-out speed. They are used as main muon triggering detectors. Gaseous parallel electrode-plates are used. Two inner layers of the RPC barrel provide triggers with low momentum threshold (range from 3 to 9 GeV). The outer third layer can trigger on high momentum (range from 9 to 35 GeV). The trigger efficiency is $\sim 97\%$ [26].

4.5.4 Thin Gap Chambers

The TGCs end-caps provide the triggering in the forward regions. It is a multi-wire proportional chamber and offers slightly better time resolution than the RPCs [26].

Chapter 5

Author's analysis on $\Upsilon \rightarrow \mu^+ \mu^-$

In this chapter, author's analysis done as part of this thesis is presented. Its topic is the study of Υ quarkonium production in heavy ion collisions at ATLAS.

Motivation

Quarkonia suppression offers a sound probe of the QGP medium creation and its temperature. The phenomenon is properly explained in Chapter 2 of the thesis. The bottomonium Υ was chosen due to its many advantages over the charmonia. Although less abundant in production, the bottomonia are more stable, considerably less prone to regeneration at LHC energies, and generally considered a cleaner probe of the QGP. The mesons' dimuon decay channel was chosen. Unlike electrons, muons do not suffer from large background. It also allows us to utilise the excellent muon detection capabilities of ATLAS.

Ambitions

The principal objective of this analysis is to reconstruct Υ dimuon invariant mass spectrum, using the data from heavy ion Pb+Pb collisions from ATLAS. Thanks to the detector great muon spectrometers, such analysis is clearly well-founded. This is, however, interesting, because to this day there has not been a single article on said analysis published by the ATLAS group.¹ Upon finding the spectrum, it is desirable to examine the effect of quarkonium suppression, if observed.

¹The group performed analysis on the Υ production in p+Pb and p+p. The results are shown and discussed in Chapter 3.

5.1. MEANS FOR ANALYSIS

5.1 Means for analysis

This part describes the data for analysis and briefly introduces the instruments used to conduct it.

5.1.1 Data

I used data from the ATLAS measurement of Pb+Pb collisions of $\sqrt{s_{\text{NN}}} = 2.76$ TeV in run 2011. The data had been already pre-processed. Two methods are used to reconstruct muons at ATLAS, *Muid* and *Staco* [29]. They combine complex algorithms to identify muons from the information given by the MS, the ID, and the calorimeters. In this analysis, I used the data given by Muid (some Staco results can be found in Appendix).

The entire dataset of almost 400 GB included approximately $4.8 \cdot 10^7$ events and $9.2 \cdot 10^7$ muons found in them, as reconstructed by Muid. The data have information on important quantities of events and muons, as well as tracks quality. The files were in the *.root* format and the data were in the form of *n-tuples*.

5.1.2 ROOT framework

The ROOT framework is an object-oriented software for data analysis of particle physics. It was developed at CERN and is written in the C++ programming language. It allows effective evaluation of large-scale data with built-in histogram and function classes as well as tools for statistical regression. It can also be used to produce graphical output of the data. Detailed information about the software can be found at [30].

5.2 Invariant mass reconstruction

This section describes the process I used to reconstruct the $m_{\mu^+\mu^-}$ invariant mass of the Υ states.

5.2.1 Methodology

The invariant mass $m_{\mu\mu}$ of a muon pair can be calculated as follows,

$$m_{\mu\mu}^2 = (E_{(1)} + E_{(2)})^2 - (\vec{p}_{(1)} + \vec{p}_{(2)})^2, \quad (5.1)$$

where E is the energy and \vec{p} the momentum. The lower-index in parentheses denotes the regarded muon.

The $m_{\mu\mu}$ has to be calculated for each muon pair in the event. Thus, three cycles run in the code — one over all events and two to select all possible non-identical muon pairs. Moreover, the $Q\bar{Q}$ can decay only into leptons of unlike sign. Therefore, we consider only oppositely-charged particles when reconstructing the signal.

Nonetheless, clearly, not every $\mu^+\mu^-$ pair comes from the quarkonia decay. Some of the pairs are uncorrelated and form a so-called *combinatorial background*. We can, however, make the assumption that such background is formed equally by the invariant mass spectrum of like-sign pairs, where there is no $Q\bar{Q}$ signal. Hence, the sought $m_{\mu^+\mu^-}$ invariant mass spectrum is computed by subtracting the $m_{\mu\mu}$ spectrum of like-sign muons from the $m_{\mu\mu}$ spectrum of the unlike-sign ones.

Feasibility of this method is demonstrated in Fig. 5.1. Significant signal of J/ψ and $\Upsilon(1S)$ can be seen. In the figure, the spectra were already subjected to other conditions, as will be explained further.

5.2.2 Cuts analysis

Certain cuts need to be applied onto the spectrum in order to improve the results. First of all, a certain level of track quality reconstruction is required. Secondly, there are cuts on the muon's momentum and pseudorapidity. These reflect the sought $\mu^+\mu^-$ pair's probable dynamic properties as well as the characteristics of the detector. It should also be noted that thanks to the algorithm's nature, events with only one muon were, rightfully, not considered.

Later in this part, I will show several distributions of the quantities I applied a cut on.

5.2. INVARIANT MASS RECONSTRUCTION

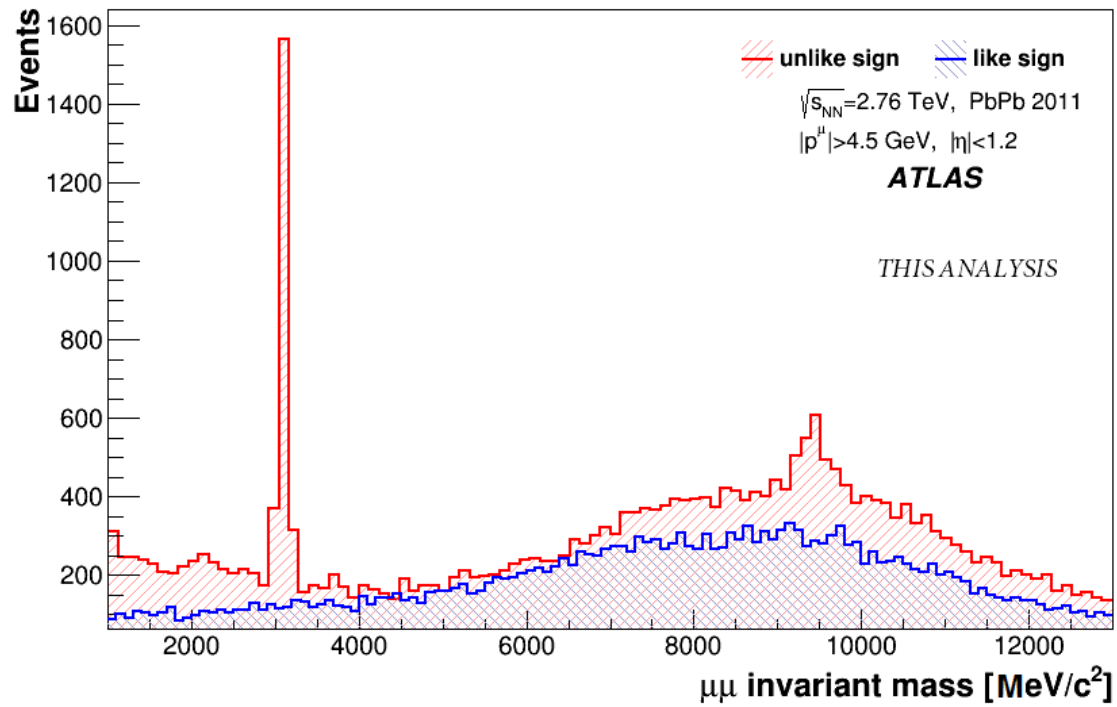


Fig. 5.1: Invariant mass spectrum of muon pairs with unlike signs and like signs. Made with shown cuts on momentum and pseudorapidity. (this analysis)

In order for the displayed distribution to be relevant, I used following method — first, I calculated $m_{\mu\mu}$ of each pair. Then only if $m_{\mu\mu}$ was in the interval from 9.0 to 10.5 GeV, I considered it. The given quantity of the first muon was then used to be included into the spectrum.

As for the track quality, I applied cuts on the values of following:

- **nBLHits = 1** — this is the amount of hits in the PD layer closest to the beam (b-layer).
- **nPixHits > 1** — the number of hits in the entire PD.
- **nSCTHits > 6** — the amount of hits in the SCT part of the ID.
- **nSCTHoles < 2** — the number of holes in the SCT detector. A hole is defined as a missing measurement when both neighbouring modules have hits. This cut could, however, be omitted.
- **isCombinedMuon = 1** and **tight = 1** — these are quality parameters of the MuId reconstruction and they have the value of 1 if the muon was identified by combining an ID and a MS track [31].

Selection of the values was based on the cuts used at ATLAS in similar analyses. The calculated distributions in considered quantities can be found in Fig. 5.2.

Cuts on the muon η and momentum $|\vec{p}|$ were also applied. The final values were chosen after computing and observing the spectra shapes and signal vs. residual background strength in different $\eta \times |\vec{p}|$ windows (find them in Appendix). Following cuts were applied:

- **pseudorapidity $|\eta| < 1.2$**
- **total momentum $|\vec{p}| > 4.5$ GeV**

The distributions in η and $|\vec{p}|$ are shown in Fig. 5.3, along with azimuthal angle ϕ (whose distribution's oddity I noticed, although did not further consider) and transverse momentum $|\vec{p}_T|$. No cuts were set on the last two in this analysis. That being said, spectra calculated with cuts on $|\vec{p}_T|$ can be found in Appendix and are almost identical.

5.2. INVARIANT MASS RECONSTRUCTION

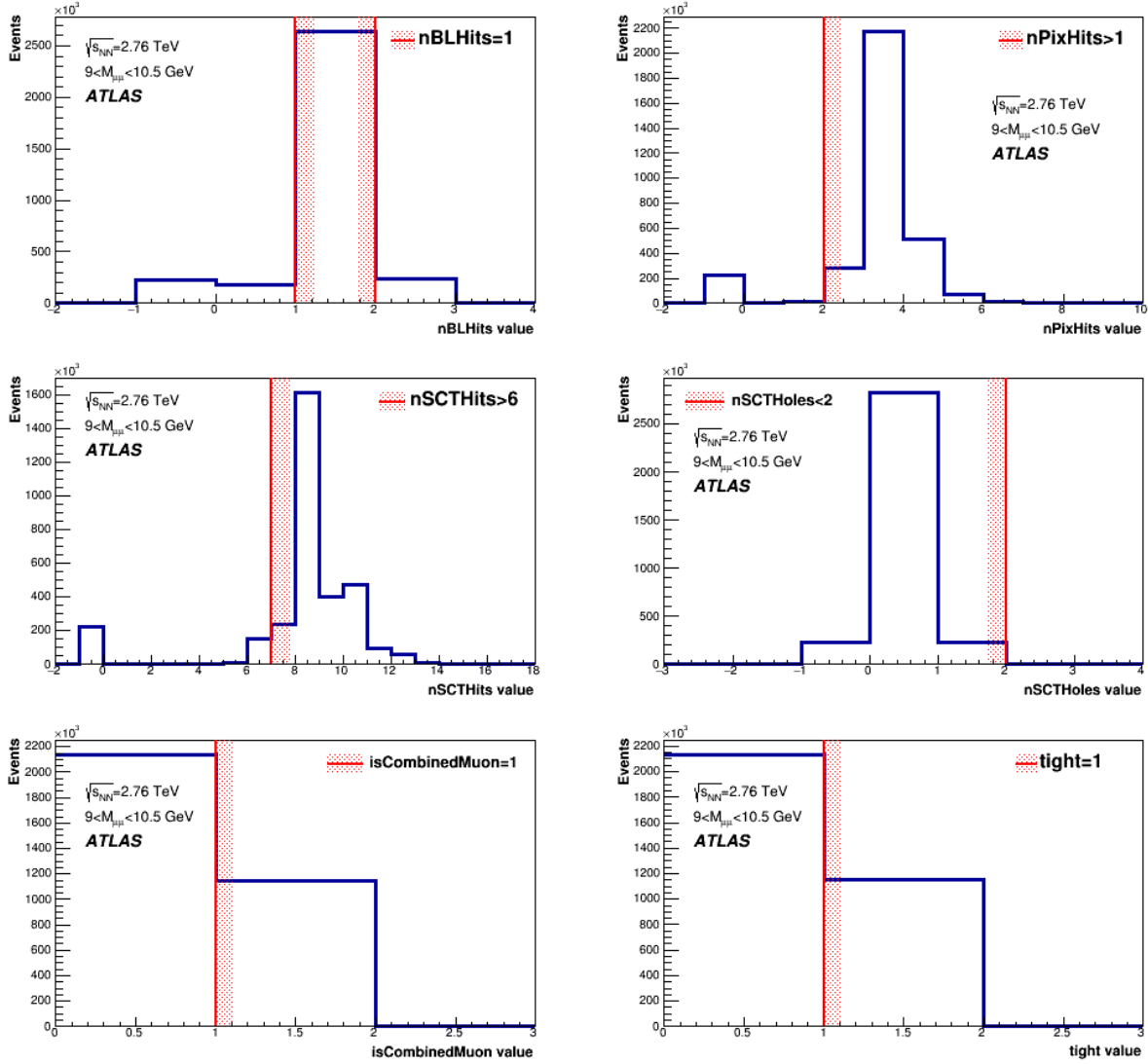


Fig. 5.2: Distribution of track quality values of the Muon reconstructed muons in the $m_{\mu\mu}$ region of Υ . Red bands indicates the threshold value and cut direction. (this analysis)

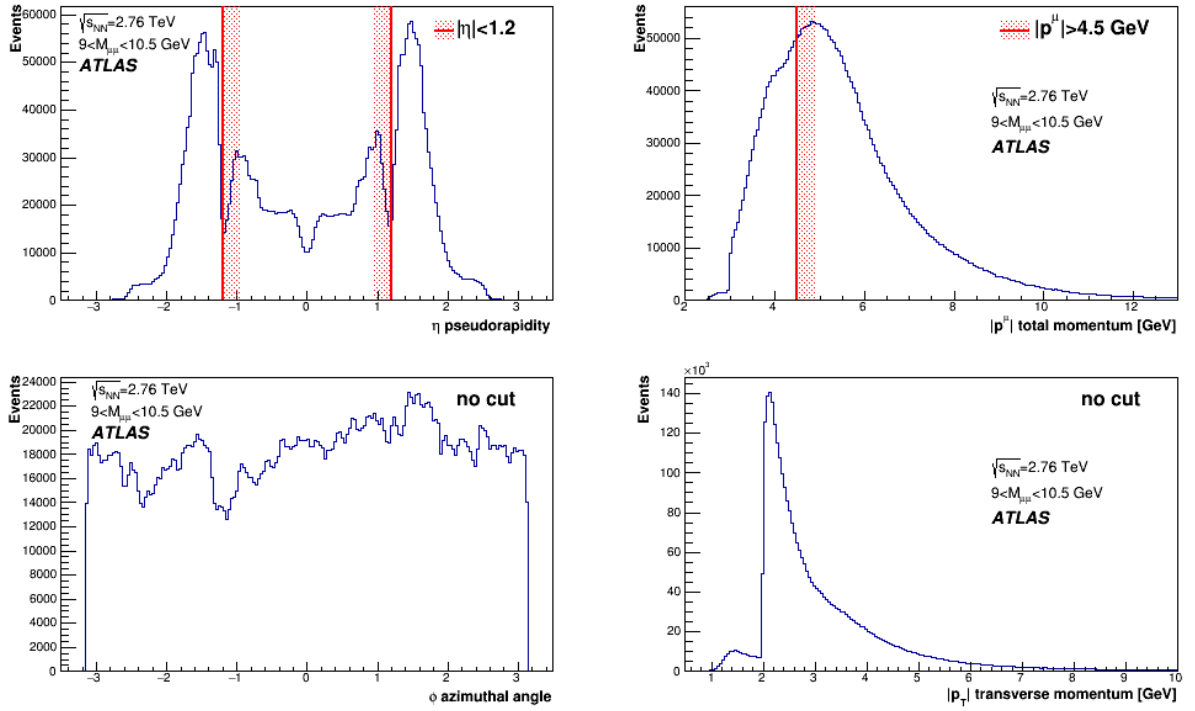


Fig. 5.3: Distribution of pseudorapidity, total momentum, azimuth, and transverse momentum of the muons in the $m_{\mu\mu}$ region of Υ reconstructed by Muid. Red bands — where shown — indicate the applied cut. (this analysis)

5.3. RESULT OF THE $M_{\mu^+\mu^-}$ SPECTRUM

5.3 Result of the $m_{\mu^+\mu^-}$ spectrum

The with cuts computed $m_{\mu^+\mu^-}$ spectrum's histogram was binned with the width of 0.2 GeV. This was chosen as the best balance between bin-to-bin fluctuations strength and the signal shape distinguishability. Each bin's y -errorbar is given by the standard error of Poisson distribution. This equals \sqrt{N} , where N is the number of counts in the bin. However, the histogram was created by the sum of two others, which must be taken into account. The final errors' correctness is ensured by the means of ROOT's *Sumw2()* method.

Standard ROOT fitting tool using the χ^2 -method was utilised to quantify the measured production. A sum of quadratic function (for the background) and three Gaussians (for the signal peaks) was chosen as the regression function. All Gaussians' centres were fixed at the mass values given by [5]. Further boundary was given for the relative widths of the $\Upsilon(2S)$ and $\Upsilon(3S)$ peaks. That ratio was taken from the ATLAS p+p results [19]. Signal significance was calculated as follows,

$$S = \frac{N}{\sqrt{N + 2B}}, \quad (5.2)$$

where N is the integrated peak without residual background and B is the integrated residual background.

Result

The reconstructed invariant mass spectrum of $\mu^+\mu^-$ pairs from Pb+Pb $\sqrt{s_{\text{NN}}} = 2.76$ TeV at ATLAS, along with fits of Υ states is displayed in Fig. 5.4. Combinatorial background of like-sign pairs was already subtracted. The red solid line, the purple dashed line, and the green dashed line represent the $\Upsilon(1S)$, $\Upsilon(2S)$, and $\Upsilon(3S)$ signals, respectively. Blue dotted line denotes the residual background. A clear $\Upsilon(1S)$ signal of significance $S_{1S} = 6.4\sigma$ can be seen, which is a great result. As for the sum of $\Upsilon(2S) + \Upsilon(3S)$, the result is lacking, with the significance $S_{2S+3S} = 2.4\sigma$.

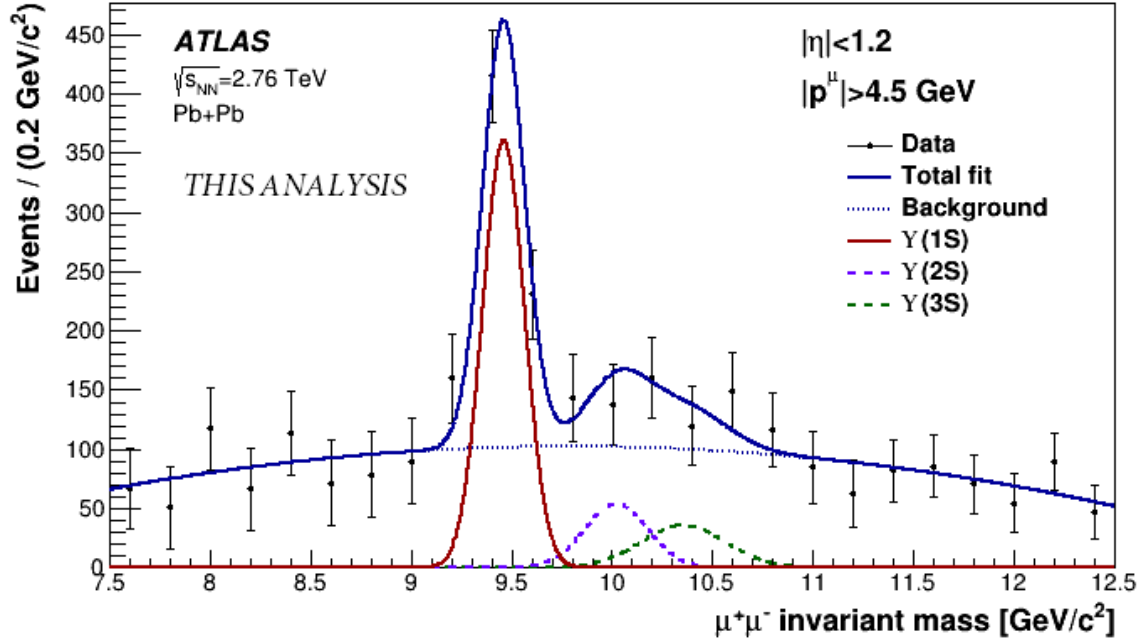


Fig. 5.4: The Υ invariant mass spectrum with a fit of the data. Lines are described in the figure's legend. (this analysis)

5.4 Centrality dependence

In order to observe the full $\Upsilon(2S)$ and $\Upsilon(3S)$ suppression, we must study the central collisions, where QGP is expected to form. In HIC at ATLAS, the centrality is usually determined by looking at the event's total transverse energy ΣE_T collected in the FCal, as proposed in [32]. The diagram used for this can be found in Fig. 5.5. The diagram shows event multiplicity as a function of ΣE_T . The function regions correspond to the event centrality and is calculated from the Glauber model. In my data, the value of event ΣE_T was named $cccEt$. The distribution of events in ΣE_T is displayed in Fig. 5.6.

Due to the modest amount statistics, I could divide the data in only two centrality regions: 0-30 % (central to semi-peripheral collisions) and 30-100 % (semi-peripheral to peripheral). This corresponded to the $cccEt$ value dividing point of 1.07 TeV [32].

5.4. CENTRALITY DEPENDENCE

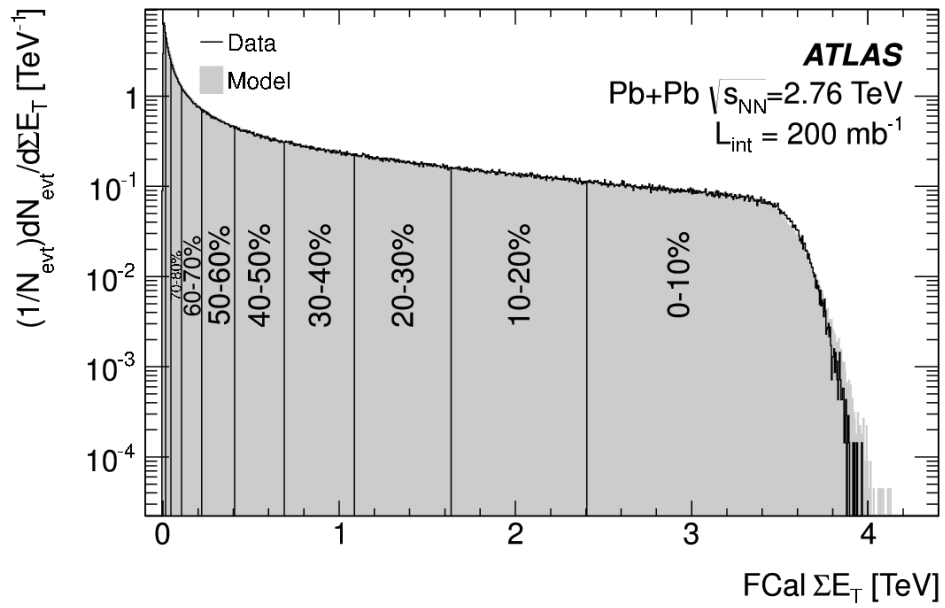


Fig. 5.5: Distribution of FCal ΣE_T with the denotation of centrality bins. Taken from [32].

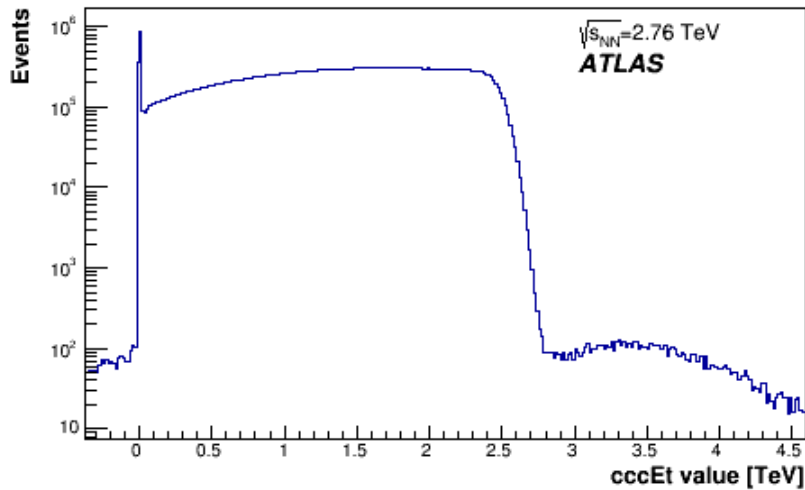


Fig. 5.6: Distribution for ΣE_T . (this analysis)

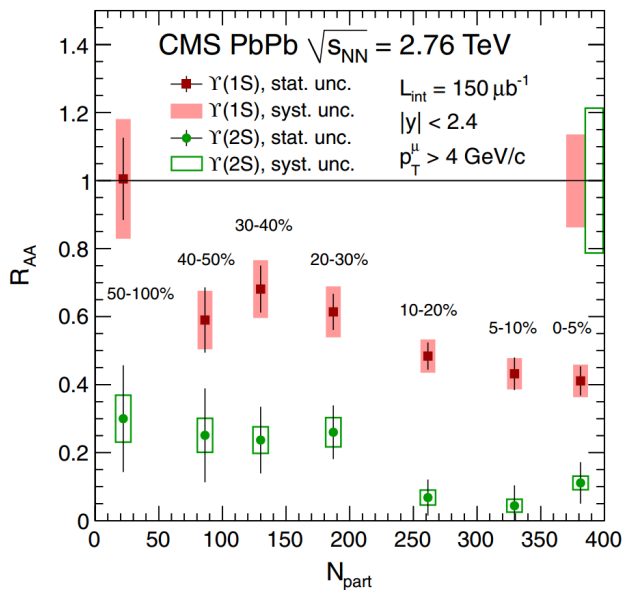


Fig. 5.7: CMS results of the R_{AA} factor dependence on multiplicity $\langle N_{part} \rangle$. Corresponding centrality regions are shown. Taken from [17].

Expectation

In CMS results on R_{AA} as function of $\langle N_{part} \rangle$ (see Fig. 5.7), we see that for multiplicities corresponding to the centrality of 0–20%, the R_{AA} for $\Upsilon(2S)$ is ~ 0.1 . On the other hand, in peripheral events, we have $R_{AA} \sim 0.3$ for the excited states. Therefore, we expect following behaviour — with the increase of multiplicity (centrality), the suppression of the excited states should be larger.

Results

The reconstructed $\mu^+\mu^-$ invariant mass spectra from Pb+Pb of $\sqrt{s_{NN}} = 2.76$ TeV at ATLAS, divided in two centrality regions, are shown in Fig. 5.8.

First, the spectrum for more central collisions (0–30%) exhibits no clear signal for $\Upsilon(2S)$ and $\Upsilon(3S)$. This is in great consistency with what was expected. In accordance with the phenomenon of quarkonia suppression (see Chapter 2), the excited states diminished due to the presence of QGP.

In the spectrum for peripheral collisions (30–100%), the signal for $\Upsilon(2S)$ and $\Upsilon(3S)$ is present! This was also anticipated. This result reflects the fact that in peripheral collisions,

5.5. OUTLOOK ON FURTHER WORK

the QGP is either of lower temperatures or not formed at all.

In summary, observation of excited states in peripheral collisions and lack thereof in more central ones is, qualitatively speaking, in great accordance with CMS results of R_{AA} as function of $\langle N_{\text{part}} \rangle$ (see Fig. 5.7).

The same fit method as in Fig. 5.4 was used. In the 30 – 100% region, one Gaussian was used to describe the sum of $\Upsilon(2S) + \Upsilon(3S)$, due to their low distinguishability. As for the $\Upsilon(1S)$ peaks, a significance of $S = 5.1\sigma$ was found for the 0 – 30% events and $S = 3.3\sigma$ for the 30 – 100% events.

5.5 Outlook on further work

Several further steps could be made in this analysis, were I to continue it. First of all, a more rigorous approach in the cuts analysis, bin width selection, and fitting would be welcomed. The method of simultaneous fit of the like-sign and unlike-sign histograms using the RooFit extension of ROOT would bring more accurate results. It is also desirable to use a more complex regression function, one including Crystal-Ball functions for the peaks.

Furthermore, the calculated raw yield would then have to be modified to account for the detector acceptance A , detector efficiency ϵ , and the branching ratio $\text{BR}_{\Upsilon(1S) \rightarrow \mu^+ \mu^-}$ of the decay. For the analysis of the former two, Monte Carlo-simulations could be utilised.

The nuclear modification factor R_{AA} could then be calculated for the Υ states in the central collisions, using the number of binary collisions N_{coll} , cross section σ^{pp} of the states in p+p collisions of equal energy, and beam luminosity. Finally, systematic and statistic uncertainties would have to be thoroughly calculated.

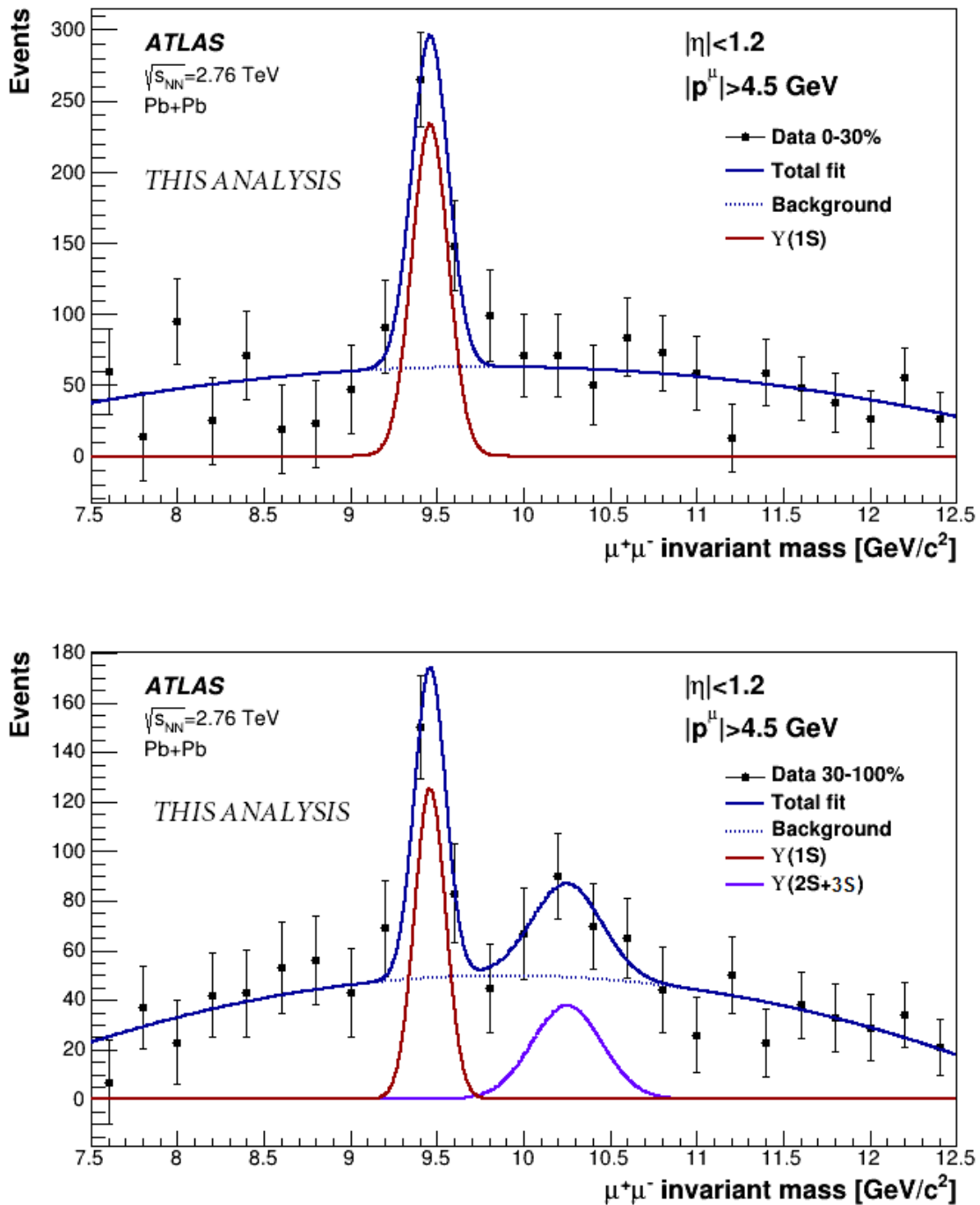


Fig. 5.8: The Υ invariant mass spectra with fits in different centrality windows. Lines are described in the legend.

Conclusion

This bachelor thesis' objective was to introduce the author's examination of HI collisions at ATLAS, namely the studies of Υ quarkonia. In its first part, introduction into particle physics and insight into the theory concerning heavy quarkonia is presented. A summary of recent Υ results is given, as well as an overview of the ATLAS experiment. Author's original analysis is covered in the later part of the thesis.

As part of this analysis, the dimuon invariant mass spectrum $m_{\mu^+\mu^-}$ was successfully reconstructed from the data on muons measured at ATLAS in 2011 in Pb+Pb collisions at $\sqrt{s_{\text{NN}}} = 2.76$ TeV. Suitable cuts on track quality and muons' η and $|\vec{p}|$ were applied after some evaluation, although a more rigorous analysis would be appropriate. A statistical regression outlining the peaks of produced $\Upsilon(1S)$, $\Upsilon(2S)$, $\Upsilon(3S)$ was performed. Clear ground state signal can be seen, nonetheless, the excited states might be difficult to tell apart.

Moreover, the spectra were evaluated in different centrality windows, which were determined by the event total transverse energy ΣE_T . The excited Υ states remained present in the peripheral events. However, none — distinguishable from background — were found in the central to semi-peripheral ones. This is consistent with the phenomenon of quarkonium suppression, which suggests the melting of the states at QGP temperatures, which are realised in the central collisions.

The analysis demonstrated the feasibility of studying HI collisions, namely heavy quarkonia, at ATLAS. The investigation done in this thesis served a great educational purpose for the author. Analysis of heavy quarkonia physics will be continued in during graduate studies.

Bibliography

- [1] CHATRCHYAN, S., et al. Observation of a new boson at a mass of 125 GeV with the CMS experiment at the LHC. *Physics Letters B*. Vol. 716, No. 1, pp. 30-61.
- [2] *Why is the Higgs discovery so significant?* [online]. Science & Technology. [ac. 02/07/16]. Available at: <http://www.stfc.ac.uk/research/particle-physics-and-particle-astrophysics/peter-higgs-a-truly-british-scientist/why-is-the-higgs-discovery-so-significant/>.
- [3] AAIJ, R., et al. Observation of $J/\psi p$ Resonances Consistent with Pentaquark States in $\Lambda_b^0 \rightarrow J/\psi K^- p$ Decays. *Physical Review Letters*. Vol. 115, No. 7.
- [4] SARKAR, S., et al. *The Physics of the Quark-Gluon Plasma A: Introductory Lectures*. Springer, c2010. ISBN 978-3-642-02286-9
- [5] EIDELMAN, S., et al. (Particle Data Group). Review of Particle Physics. *Physical Letters B*. Vol. 592, No. 1.
- [6] VOGT, R. *Ultrarelativistic Heavy-Ion Collisions*. Elsevier, 1st edition, c2007. ISBN 9780444521965
- [7] WONG, C. *Introduction to High-Energy Heavy Ion collisions*. Utopia Press, 1st edition, c1994. ISBN 978-981-02-0263-7
- [8] MATSUI, T., SATZ., H. J/ψ Suppression by Quark-Gluon Plasma Formation. *Physical Letters B*. Vol. 178, pp. 416-422
- [9] ANDRONIC, A., et al. Heavy-flavour and quarkonium production in the LHC era: from proton proton to heavy-ion collisions. *Eur.Phys.J.* C76, No. 3.
- [10] ADARE, A., et al. (PHENIX Collaboration). Measurement of $\Upsilon(1S + 2S + 3S)$ production in $p + p$ and Au+Au collisions at $\sqrt{s_{NN}} = 200$ GeV. *Phys. Rev.* C91. No. 2.

BIBLIOGRAPHY

- [11] ESKOLA, K.J., et al. EPS09: A New Generation of NLO and LO Nuclear Parton Distribution Functions. *JHEP 0904 065*.
- [12] KRZYWICKI, A., et al. Does a nucleus act like a gluon filter? *Physics Letters B*. Vol. 85, No. 4, pp. 407-412.
- [13] ARLEO, F., PEIGNE, S. Heavy-quarkonium suppression in p-A collisions from parton energy loss in cold QCD matter. *JHEP 1303 122*
- [14] DIGAL, S., PETRECZKY, P., SATZ, H. Quarkonium feed down and sequential suppression. *Physical Review D*. Vol. 64, No. 9
- [15] DAS, I. Upsilon production measurements in pp, p-Pb and Pb-Pb collisions with ALICE. *Quark Matter 2015* [online]. 2015. [ac. 02/07/16]. Available at: <https://indico.cern.ch/event/355454/contributions/838966/>
- [16] ABELEV, B., et al. (ALICE). Suppression of $\Upsilon(1S)$ at forward rapidity in Pb-Pb collisions at $\sqrt{s_{NN}} = 2.76$ TeV. *Physical Letters B*. Vol. 738, pp. 361-372.
- [17] CHATRCHYAN, S., et al. (CMS). Observation of Sequential Υ Suppression in PbPb Collisions. *Phys. Rev. Lett.* Vol.109, No. 22.
- [18] ABELEV, B., et al. (ALICE). Production of inclusive $\Upsilon(1S)$ and $\Upsilon(2S)$ in p-Pb collisions at $\sqrt{s_{NN}} = 5.02$ TeV. *Phys. Lett. B*. Vol. 740, pp. 105-117
- [19] ATLAS collaboration. Measurement of $\Upsilon(nS)$ production with p+Pb collisions at $\sqrt{s_{NN}} = 5.02$ TeV and pp collisions at $\sqrt{s} = 2.76$ TeV [online]. 2015. [ac. 02/07/16]. Available at: <http://cds.cern.ch/record/2055266>.
- [20] RONGRONG, M. J/ψ and Υ measurements via the di-muon channel in Au + Au collisions at $\sqrt{s_{NN}} = 200$ GeV with the STAR experiment [online]. 2015. [ac. 02/07/16]. Available at: <https://arxiv.org/abs/1512.08713>
- [21] ADAMCZYK, L., et al. (STAR). Suppression of Υ production in d+Au and Au+Au collisions at $\sqrt{s_{NN}}=200$ GeV. *Phys. Lett. B*. Vol. 735, pp. 127-137. Erratum: *Phys.Lett.B*. Vol. 743, pp. 537-541.
- [22] CERN's Accelerator Complex. In: *CERN Document Server* [online] c2013-2016 CERN. [ac. 02/07/16]. Available at: <http://cds.cern.ch/record/1621583/>

- [23] Computer generated image of the whole ATLAS detector. In: *CERN Document Server* [online] c2008 CERN. [ac. 02/07/16]. Available at: <http://cds.cern.ch/record/16095924/>
- [24] Computer generated image representing how ATLAS detects particles. In: *CERN Document Server* [online] c2013 CERN. [ac. 02/07/16]. Available at: <http://cds.cern.ch/record/1505342/>
- [25] Computer generated image of the ATLAS inner detector. In: *CERN Document Server* [online] c2008 CERN. [ac. 02/07/16]. Available at: <http://cds.cern.ch/record/1095926/>
- [26] AAD, G., et al. (ATLAS). The ATLAS Experiment at the CERN Large Hadron Collider. *ResearchGate*. [online]. 2008. [ac. 02/07/16]. Available at: https://www.researchgate.net/publication/44710635_The_ATLAS_Experiment_at_the_CERN_Large_Hadron_Collider
- [27] Computer generated image of the ATLAS calorimeter. In: *CERN Document Server* [online] c2008 CERN. [ac. 02/07/16]. Available at: <http://cds.cern.ch/record/1095927/>
- [28] Computer generated image of the ATLAS Muons subsystem. In: *CERN Document Server* [online] c2008 CERN. [ac. 02/07/16]. Available at: <http://cds.cern.ch/record/1095929/>
- [29] RESENDE, B. Muon identification algorithms in ATLAS. In: *CERN Document Server* [online] 2009 CERN. [ac. 02/07/16]. Available at: <http://cds.cern.ch/record/1209632/>
- [30] *ROOT*. [software]. Data Analysis Framework. [opensource]. [ac. 02/07/16]. Available at: <http://root.cern.ch>
- [31] HENRICHS, A.C. *Top Quark Pair Production*. Springer, 1st edition, c2014. ISBN 978-3-319-01487-6
- [32] STEINBERG, P. Recent Heavy Ion Results with the ATLAS Detector at the LHC [online]. 2011. [ac. 02/08/16]. Available at: <https://arxiv.org/abs/1110.3352>

A Fit results

The following regression function was used to fit data in Fig. 5.4,

$$f(x) = a + b \cdot (x - c)^2 + d \cdot \exp \left[-\frac{(x - \mu_1)^2}{2e^2} \right] + f \cdot \exp \left[-\frac{(x - \mu_2)^2}{2g^2} \right] + h \cdot \exp \left[-\frac{(x - \mu_3)^2}{2j^2} \right] .$$

Following parameters were obtained:

| | | | |
|---------------|---------------------------------|---------------------------------|---------------------------------|
| fit parameter | a | b | c |
| value | $(1.02 \pm 0.08) \cdot 10^2$ | $(-6.87 \pm 2.50) \cdot 10^0$ | $(9.80 \pm 0.30) \cdot 10^0$ |
| fit parameter | d | e | f |
| value | $(3.60 \pm 0.46) \cdot 10^2$ | $(1.05 \pm 0.15) \cdot 10^{-1}$ | $(5.37 \pm 3.10) \cdot 10^1$ |
| fit parameter | g | h | i |
| value | $(1.57 \pm 0.70) \cdot 10^{-1}$ | $(3.58 \pm 2.20) \cdot 10^1$ | $(2.10 \pm 1.00) \cdot 10^{-1}$ |

Tab. 1: Fit parameters results for fit in Fig. 5.4.

B Staco reconstructed quantities

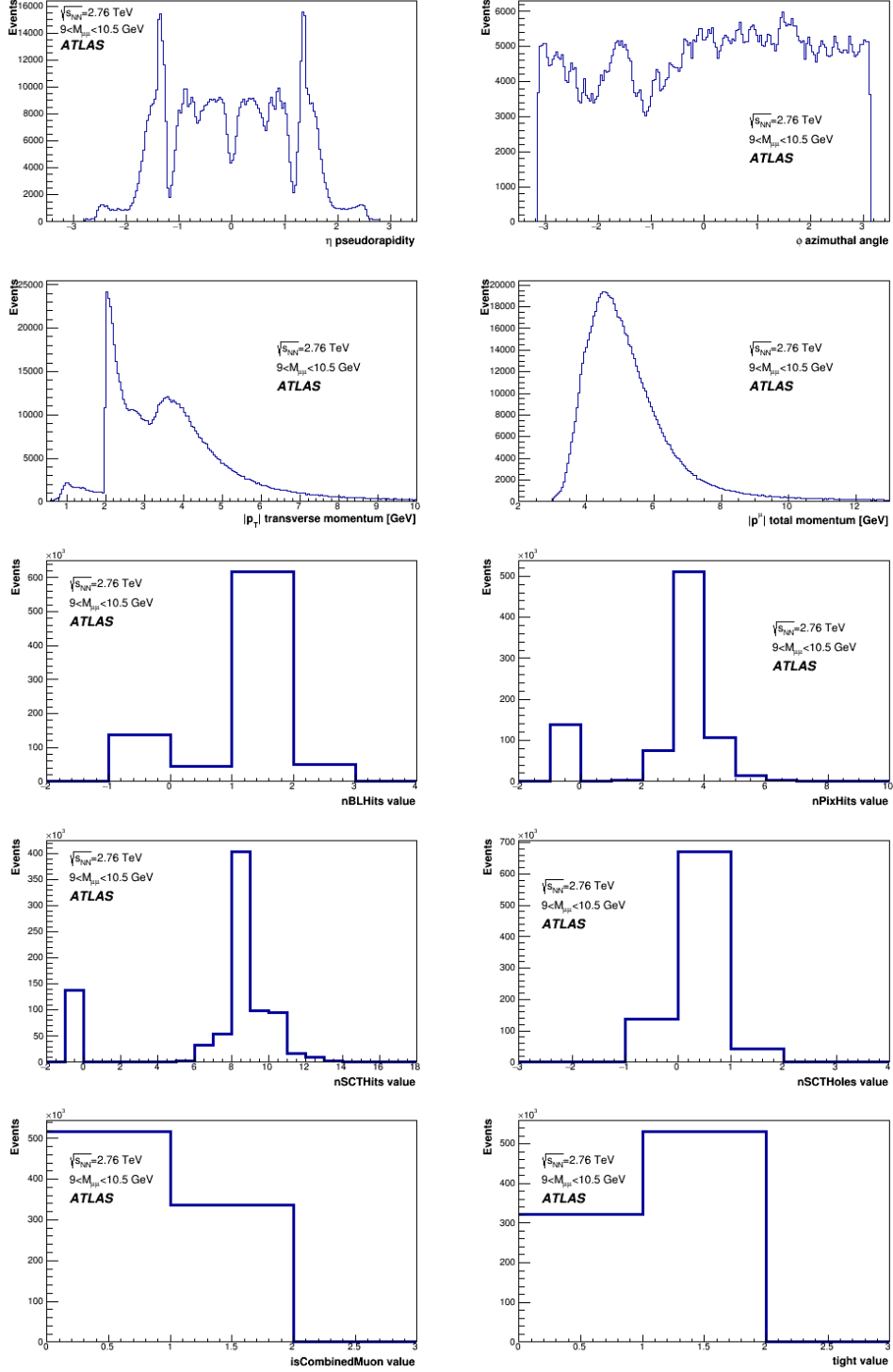


Fig. 1: Distribution of quantities reconstructed by the Staco algorithm.

C Invariant mass spectra dependence on η vs. $|\vec{p}_T|$

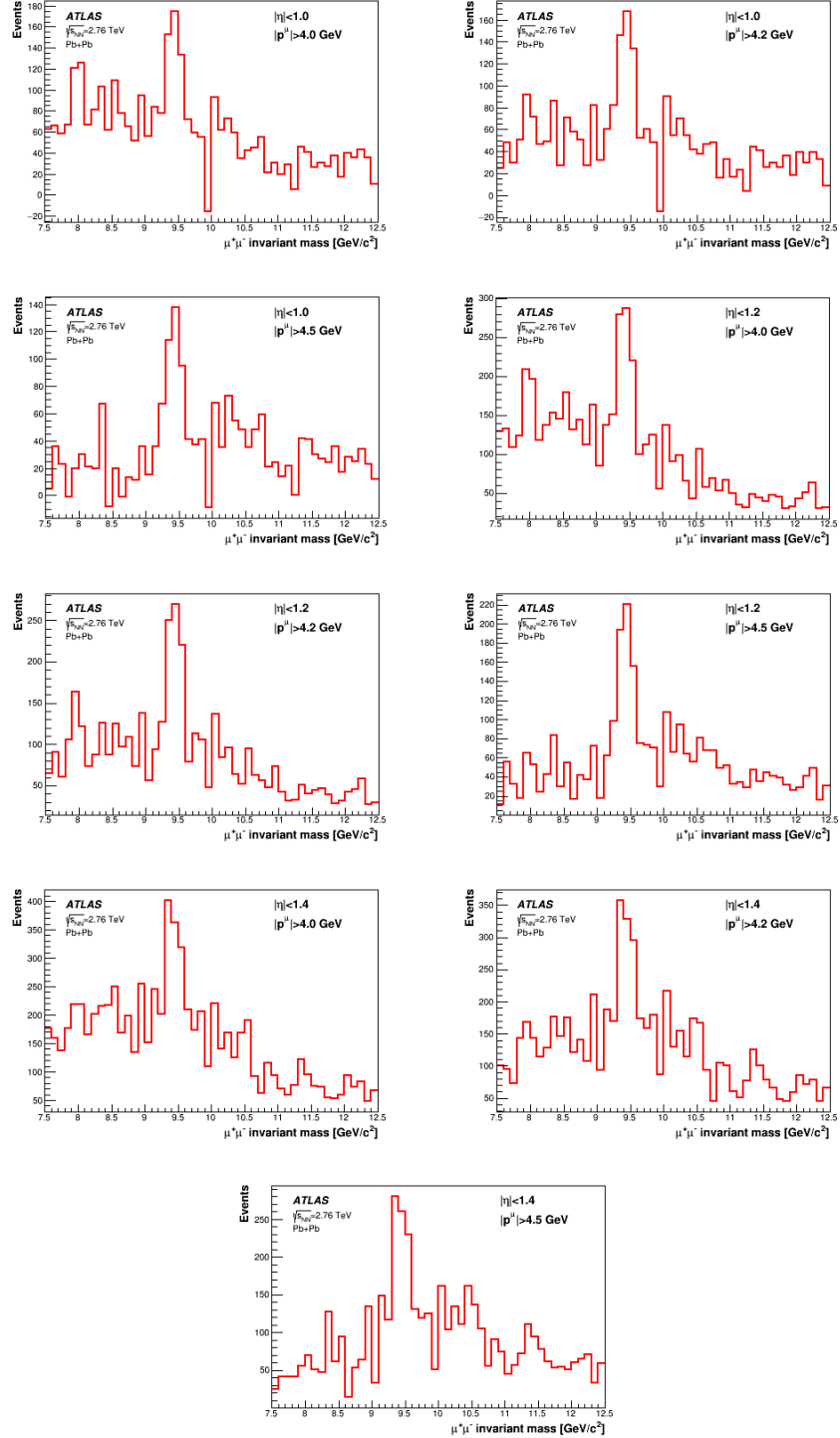


Fig. 2: Invariant mass spectra computed in different η and $|\vec{p}_T|$ regions.

D Invariant mass spectra with cuts on p_T

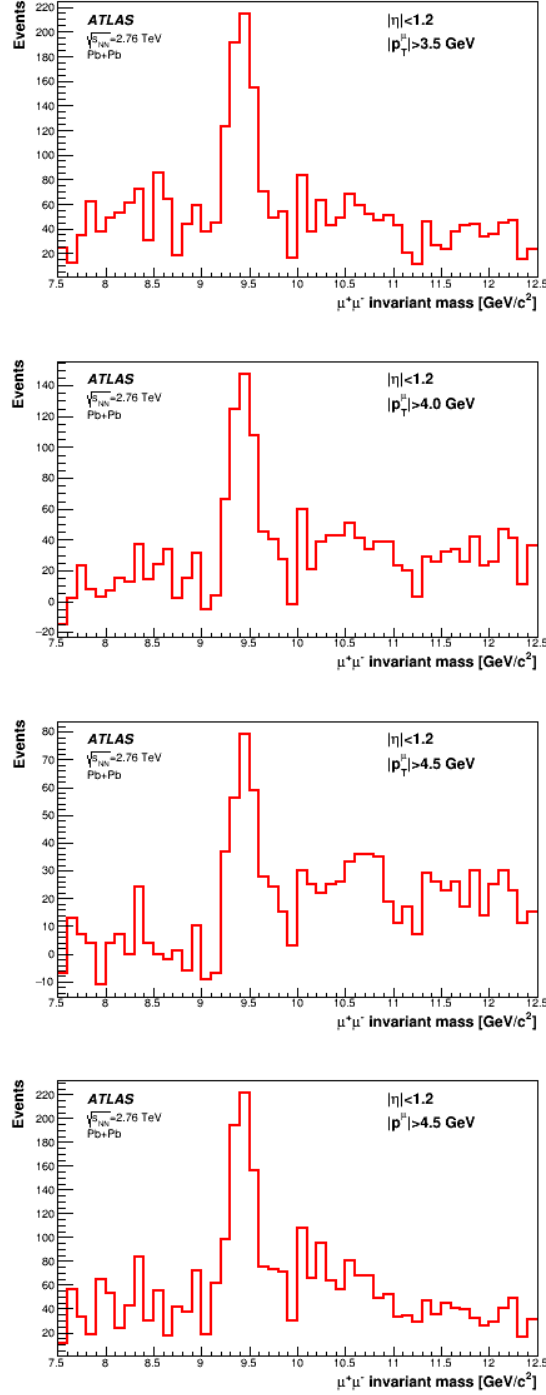


Fig. 3: Invariant mass spectra calculated with cuts on p_T . Case with cut on $|p|$ is shown for comparison.